THE ASTROPHYSICAL JOURNAL, 468:398–417, 1996 September 1

ELECTRON TIME-OF-FLIGHT DISTANCES AND FLARE LOOP GEOMETRIES COMPARED FROM *CGRO* AND *YOHKOH* OBSERVATIONS

MARKUS J. ASCHWANDEN
Department of Astronomy, University of Maryland, College Park, MD 20742; markus@astro.umd.edu
MEREDITH J. WILLS
Harvard-Smithsonian Center for Astrophysics, 60 Garden Street, Cambridge, MA 02138
HUGH S. HUDSON
Institute for Astronomy, University of Hawaii, Honolulu, HI 96822
TAKEO KOSUGI
National Astronomical Observatory, Mitaka, Tokyo 181, Japan
AND
RICHARD A. SCHWARTZ
Hughes STX, NASA Goddard Space Flight Center, Code 682, Greenbelt, MD 20771
Received 1996 January 24; accepted 1996 March 27

ABSTRACT

The distance between the coronal acceleration site and the chromospheric hard X-ray (HXR) emission site can be determined from velocity-dependent electron time-of-flight (TOF) differences in the framework of the thick-target model. We determine these electron TOF distances l with relative time delay measurements in the 30–300 keV energy range, using 16 channel data from BATSE/*CGRO* for the eight largest flares simultaneously observed with *Yohkoh*. We filter the HXR fine structure from the smoothly varying HXR flux with a Fourier filter in order to separate competing time delays. In the *Yohkoh*/HXT images we identify the corresponding flare loops that show ≥ 30 keV HXR footpoint emission and project the electron TOF distances into the loop plane, assuming a semicircular shape (with radius r). The flare loop radii vary in the range of $r = 5600$–$17{,}000$ km. In all eight flares we find that the *projected electron TOF distance* l' exceeds the loop half-length $s = r(\pi/2)$, with a scale-invariant ratio of $l'/s = 1.3 \pm 0.2$. Projecting the electron TOF distances onto an open field line that extends to the cusp region above the flare loop, we find an average ratio of $h/r = 1.7 \pm 0.4$ for the height h of the acceleration site. This geometry is compatible with acceleration mechanisms operating in the cusp region, perhaps associated with magnetic reconnection processes above the flare loop. Alternatively, acceleration sites inside the flare loop cannot be ruled out (since $l'/s < 2$), but they do not provide a natural explanation for the observed length ratio l'/s. Large-scale electric DC field acceleration mechanisms are found to be less suitable to explain the observed HXR timing and pulse durations.

Subject headings: acceleration of particles — radiation mechanisms: nonthermal — Sun: corona — Sun: flares — Sun: X-rays, gamma rays

1. INTRODUCTION

The basic idea of this study is to determine the length of electron time-of-flight (TOF) paths during solar flares on one hand, by means of high-precision time delay measurements between different hard X-ray (HXR) energies, and to compare these TOF distances with simultaneous HXR images of the relevant flare loops on the other hand. By selecting flares with HXR emission from loop footpoints, the measured TOF distance corresponds then to the spatial separation between acceleration sites and the HXR emission at the chromospheric loop footpoints. With this method we attempt to pinpoint the so far elusive location of particle acceleration sites with respect to the flare loop geometry. In particular, we hope to gain insight into the long-standing question whether the primary energy release region and the associated acceleration mechanisms are located *inside* or *outside* flare loops, in the latter case perhaps in the cusp. This is crucial information that often represents a fundamental assumption in many theoretical flare models, but could not be constrained rigorously by observations so far.

Since the creation of flare models with putative energy release sites near (or above) loop tops (e.g., see reviews of Dennis 1985, 1988 and Dennis & Schwartz 1989, and references therein; or theoretical models by Sturrock 1966; Kopp & Pneuman 1976; Tsuneta 1995a) and the observational evidence of energy-loss sites near footpoints (Hoyng et al. 1981; Duijveman, Hoyng, & Machado 1982; Takakura, Tanaka, & Hiei 1984; Sakao 1994), a picture that emerged from numerous HXR observations by *Hinotori*, *SMM*, and *Yohkoh*, the theoretical basis for estimating electron TOF effects was essentially provided and considered in some theoretical models (Emslie 1983). Observational verification has not been pursued until recently. Part of the difficulty can be attributed to the smallness of the expected effect ($\lesssim 100$ ms), which might have discouraged observers or even cast doubts whether this effect is measurable (Emslie & Mehta 1994). The first positive measurement of energy-dependent HXR delays attributable to electron TOF differences was found in three flares observed with a time resolution of 128 ms with the Hard X-Ray Burst Spectrometer (HXRBS) on board the *Solar Maximum Mission* (*SMM*) spacecraft (Aschwanden et al. 1995a). A breakthrough in the measurement of electron TOF differences occurred only recently from the detailed timing

analysis of high time resolution (64 ms) data from the most sensitive Burst and Transient Source Experiment (BATSE) detectors on board the *Compton Gamma Ray Observatory* (*CGRO*). A statistical study of all burst-trigger data in 640 solar flares revealed a systematic time delay of $\tau \pm \sigma_\tau = 17 \pm 17$ ms for background-subtracted HXR pulses at 25–50 keV with respect to 50–100 keV (Aschwanden, Schwartz, & Alt 1995b, hereafter Paper I). The accurate measurement of such small timing effects beyond the instrumental time resolution can be accomplished with cross-correlation techniques and interpolation schemes in time delay subintervals, but requires a careful treatment of systematic errors and statistical uncertainties due to Poisson noise, aliasing effects, incomplete sampling, and subtraction of unwanted time structures with opposite timing characteristics. A systematic investigation of these effects was performed in a second study (Aschwanden & Schwartz 1995, hereafter Paper II), leading to a representative overview of four different time delay regimes for ≥ 25 keV HXR emission, which could be attributed to four different physical mechanisms: (1) TOF differences in the chromospheric thick-target model ($0 \lesssim \tau \lesssim 100$ ms), (2) energy-loss time differences by coronal thin- or thick-target emission (-100 ms $\lesssim \tau \lesssim 0$), (3) coronal trapping mechanisms (-10 s $\lesssim \tau \lesssim -0.1$ s), and (4) convolution with thermal effects ($0.1 \lesssim \tau \lesssim 10$ s). An important discovery was that these often simultaneously occurring physical mechanisms can be disentangled in HXR data if the relevant time structures are properly filtered. For instance, in one of Masuda's flares (Masuda 1994; Masuda et al. 1994, 1995), on 1992 January 13, HXR pulses with a small modulation depth were found to exhibit small delays ($\tau_P = 40$–220 ms) that are characteristic for electron TOF differences, while the smoothly varying HXR flux showed a much larger delay ($-\tau_S = 2.1$–6.6 s) of opposite sign that was found to be consistent with trapping times in terms of collisional deflection (Aschwanden et al. 1996, hereafter Paper III). Further progress in the reliability of electron TOF measurements was made by the development of an accurate inversion method of HXR time delays, which are measured from time-dependent HXR spectra, produced by a convolution of electron injection spectra with electron propagation effects, the bremsstrahlung cross section, and the detector response function (Aschwanden & Schwartz 1996, hereafter Paper IV). Additional timing effects can potentially confuse the measurement of electron propagation, e.g., energy-dependent acceleration timescales, but an attempt of fitting five different acceleration scenarios to observed HXR delays over an energy range of 40–350 keV in a well-observed flare failed to show any appreciable effect of acceleration timescales (Aschwanden 1996, hereafter Paper V). Based on the systematic investigations in this previous work (Papers I–V) we are now in the position to determine electron TOF distances with unprecedented accuracy for the selection of flares simultaneously observed with *Yohkoh* presented in this study.

The spatiotemporal link in this study is the combination of HXR timing measurements from *CGRO* with flare loop geometries inferred from images recorded with the Hard X-Ray Telescope (HXT) and the Soft X-Ray Telescope (SXT) on board the *Yohkoh* spacecraft. A large number of flare loops have been observed with these two instruments, complementing each other nicely in mapping thermal and nonthermal HXR sources, as well as the heated flare plasma that fills up magnetically connected flare loops. Sakao (1994) cataloged the morphology of HXR sources and found that 40% of the flares show double footpoints. These flares are the most unambiguous ones to relate to TOF distances. Other flares show only one single HXR source, which may be associated with one of the footpoints if the loop has a strongly asymmetric magnetic mirror ratio, or it may be located in the coronal part of the flare loop if the electron density is sufficiently high to warrant collisional energy loss inside the flare loop. From the delay characteristics we should be able clearly to distinguish between these two cases, because the energy-dependent time delay is expected to have an opposite sign for the two cases (Paper II). Sakao (1994) found also more complicated sources with multiple components in 30% of the flares. These cases may be ambiguous for the localization of acceleration sites with our TOF analysis. We will employ coregistered SXT and HXT images to obtain clarity on the magnetic geometry.

The strategy of this study is to select, among the complete data set of flares observed simultaneously with *CGRO* and *Yohkoh*, those with the highest HXR count rates ($\geq 10^5$ counts s^{-1}). The largest flares provide the best signal-to-noise ratio for high-precision timing measurements and provide the largest energy range over which the functional shape of the energy-dependent timing can be determined. By the same token, the flares with the highest count rates are also most suitable for image reconstruction with HXT and are therefore most likely to be subject of other studies with *Yohkoh* data. In fact, we realize that 10 out of the 11 largest flares selected for this study have also been analyzed by Sakao (1994) or other workers (Sakao et al. 1992; Hudson et al. 1992; Canfield et al. 1992; Kane et al. 1993a, 1993b; McTiernan et al. 1994; Kawabata et al. 1994a, 1994b; Culhane et al. 1993; Wuelser et al. 1994; Inda-Koide et al. 1995). Only one single *Yohkoh* flare has been analyzed so far under the aspect of electron TOF distance measurements, yielding the surprising result that the location of the electron acceleration site was inferred in an altitude a factor of ≈ 3 higher than the apex of the bright SXR flare loop (Paper III). In this study we are interested to evaluate whether this height ratio is typical or exceptional in flares.

This paper is organized into two main data analysis parts, containing the analysis of TOF distances from BATSE/*CGRO* data (§ 2) and the analysis of flare loop geometries from *Yohkoh* data (§ 3). In the Discussion (§ 4) we summarize the observational constraints for acceleration models (§ 4.1) and evaluate which theoretical acceleration models are consistent with our HXR timing measurements (§§ 4.2–4.3). Our conclusions follow in § 5.

2. *CGRO* DATA ANALYSIS

2.1. *Instrumentation and Observations*

We analyze solar flare data observed with the Burst and Transient Source Experiment (BATSE) on board *CGRO*. *BATSE* consists of eight Large Area Detectors (LADs), placed at the eight corners of the spacecraft, each with a sensitive area of 2025 cm^2. The LAD detectors are made of NaI scintillation crystals, uncollimated in the forward hemisphere and passively shielded in the rear hemisphere. The front of the LAD is covered with plastic scintillation detectors in anticoincidence to reduce the background due to charged particles. Descriptions of the detectors can be found in Fishman et al. (1989, 1992).

The ≥ 25 keV HXR count rates from the eight detectors

are processed in different modes with various time resolutions and energy bandwidths. Fast readout with a time resolution of ≤ 64 ms is activated after a burst trigger occurs, requiring a significant increase in count rate (on a threshold nominally set at 5.5 σ) on one of three timescales: 64 ms, 256 ms, and 1024 ms. The discriminator rates in channels 2 and 3 ($\approx$60–325 keV) are used, and at least two detectors must exceed the threshold for a burst trigger to occur. The count rates are then summed from the triggered two detectors with high time resolution for a limited time period. This time period consists of 4096 data points with 64 ms (totaling to $\approx$4 minutes) for 4 channel spectra (*Discriminator Science Data (DISCSC)* data type), or of 2048 data points with 16 ms plus 2048 data points with 64 ms (totaling to $\approx$3 minutes) for 16 channel spectra [medium energy resolution (MER) data type]. The relative time synchronization of the channel readouts is better than a few microseconds (G. Fishman 1995, private communication), while our best relative delay measurements have statistical uncertainties of $\gtrsim$2 ms. The detector response function of the 16 channel MER spectra is shown in Paper IV.

2.2. *Data Set*

In this study we are using MER 16 channel data because of the higher number of energy channels than the *DISCSC* 4 channel data. We rebin the first 2048 data points with 16 ms time resolution to 512 data points with 64 ms, obtaining a total of 2560 data points with a uniform time resolution of 64 ms for each burst trigger event, which are in this form more suitable for cross-correlations. In some of the MER data records we detected data gaps that brought the 16 channels out of synchronization, because the data string wraps around from channel to channel. We found that the data gaps always had a fixed length in multiples of 256 data points, and from this we were able to restore the correct time order using the synchronized time marks in each channel resulting from the count rate discontinuities at the begin/end of the burst trigger or at the switch time between different time resolutions (16 ms/64 ms). We cross-checked the corrected MER data with the redundant *DISCSC* data. There is no danger that these time corrections could affect our timing results obtained from the cross-correlation between different channels, because the inferred time delays in the order of $\lesssim$100 ms correspond only to shifts of 1–2 data points, while the time corrections were done in multiples of 256 data points.

2.3. *Flare Selection*

BATSE has recorded some 4000 solar flares during the first 4 years since the launch date in 1991 April. All these flares were registered in a continuous recording mode with a basic time resolution of 1.024 s, while some 700 flares were sufficiently strong to cause a burst trigger. These were recorded with a higher time resolution ($\leq$64 ms). We screened these 700 burst-trigger events for simultaneous coverage with *Yohkoh* flare mode and identified 140 commonly observed events. In this study we select only the largest of these flares, with a *BATSE* peak count rate of $C \geq 10^5$ counts s^{-1}, yielding a sample of 17 events. We analyze the 11 events from the 1991–1992 period. The other six events from the 1993–1995 period are left for later analysis because of data access problems. From the 11 selected events we find two of them unusable for our analysis; one of them (1991 October 27, 0537 UT) suffered from pulse pile-up to such a strong degree that the dead-time overcorrection led to flux deficiencies in the higher energy channels during flux enhancements in the lower energy channels; the other event (1992 September 11, 0604 UT) had a data gap that extended over 15 of the 16 channels. Other events with smaller data gaps or less severe pulse-pileup effects could still be analyzed. So we are left with nine analyzable events.

Because we are interested in electron TOF measurements in this study, a necessary requirement is that the relevant time structures have to show a positive time delay for the lower HXR energies with respect to higher energies, while negative delays represent unphysical solutions. We were able to identify time structures with positive time delays that qualify for electron TOF differences in eight of the nine analyzable events . These eight large events are listed in Table 1 and are analyzed in detail in this study. The other large event (1991 December 30, 2306 UT) belongs to a different time delay regime and requires another physical model than electron TOF effects (see description of four delay regimes and associated physical models in Paper II). The ratio of events with positive to negative delays is found here to be even higher ($\approx$90%) than in a representative study of 622 flares in Paper II ($\approx$76%) because we filter out the slowly varying smooth HXR flux here to suppress competing timing effects (see next section).

2.4. *Time Structures*

Time profiles of the eight analyzed flares are shown in Figure 1 for a subset of the 16 MER channels that were found to be useful for time delay measurements. The lowest MER channel 1 was always discarded because its response function is not well understood. We also omitted those high-energy channels with unsufficient count rates for accurate delay measurements. We avoided some channels that

TABLE 1

CGRO/BATSE Hard X-Ray Parameters of Eight Analyzed Flares

Flare Number	Date	Start Time (UT)	Time Range (s)	Time Filter (s)	Autocorrelation Width w_p (s)	Peak Counts (counts s^{-1})	Energy Channels	Spectral Index γ	*GOES* Class
1	91/11/09	2051:44.3	0–70	3.6	1.58	2.4×10^5	2–6	3.27	M1.4
2	91/11/10	2005:31.4	0–164	2.5	0.88	4.1×10^5	2–9	3.64	M7.9
3	91/11/15	2234:36.6	0–80	1.5	1.01	13.0×10^5	2–6	4.01	X1.5
4	91/12/04	1743:02.5	0–164	2.0	0.92	1.0×10^5	2–8	4.08	M4.1
5	91/12/15	1832:14.8	5–70	3.0	0.96	4.9×10^5	4–10	2.75	M1.4
6	91/12/26	1047:35.4	26–150	1.0	0.40	7.4×10^5	2–8	3.77	M4.6
7	91/12/26	2135:59.1	0–164	2.5	1.19	2.4×10^5	3–7	4.12	M4.2
8	92/02/14	2306:48.9	0–100	1.8	0.75	11.0×10^5	6–10	3.33	M7.0

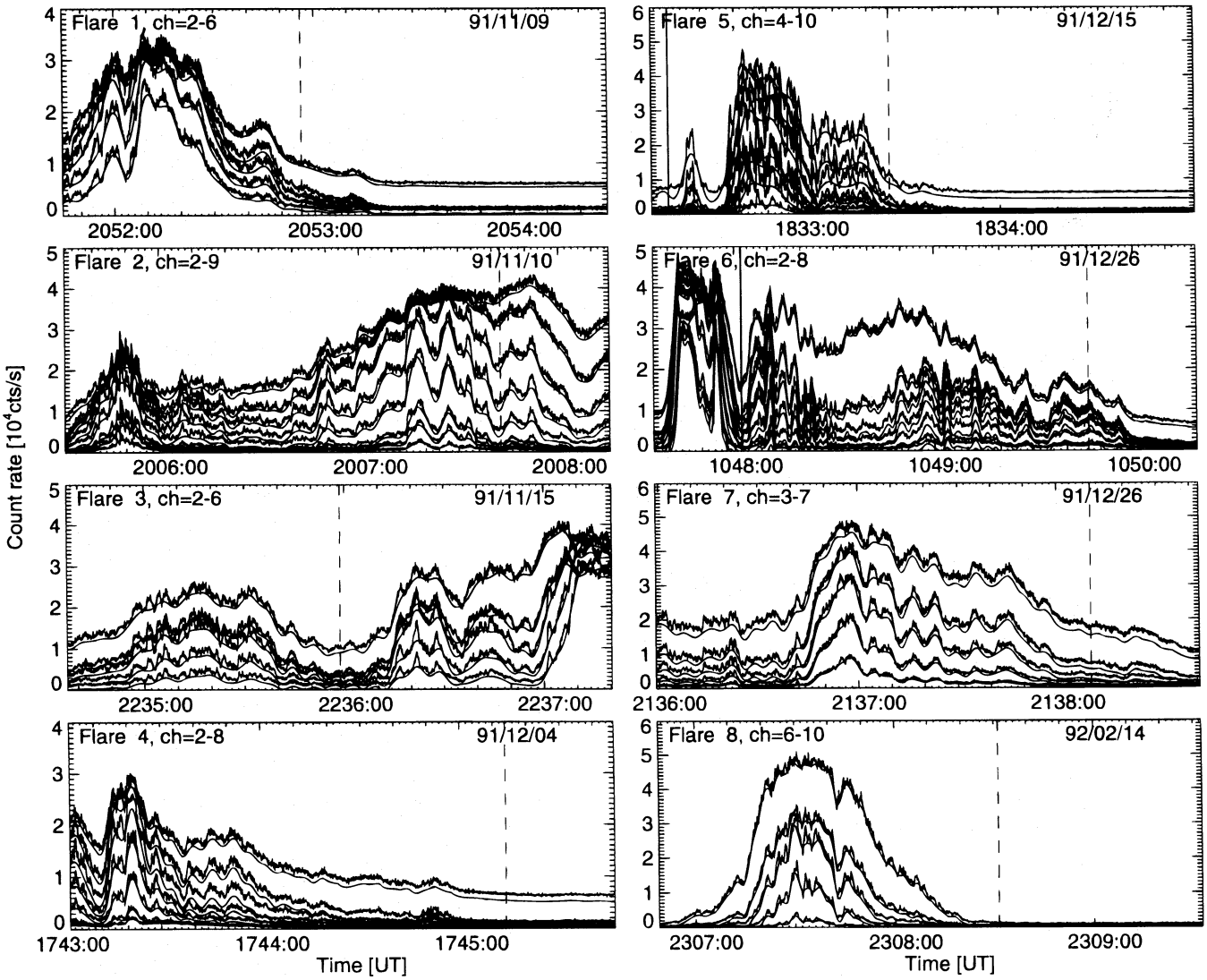

FIG. 1.—Time profiles of the analyzed eight flares (Table 1) recorded with BATSE in the 16 channel medium energy resolution (MER) mode with a time resolution of 64 ms. The analyzed fine structure was subtracted from the smoothly varying HXR flux (indicated with smooth profiles) by a FFT filter. All frames have the same duration of 163.84 s. If the analyzed interval does not include the entire interval, the start is indicated with a thin vertical line and the end with a dashed vertical line. The numbers of the selected channels are indicated at the top left.

were affected by pulse pile-up (e.g., channels 2–5 in flare 8) or channels with missing data. Some low-energy channels (2, 3) were not used because the fine structure was less correlated with higher channels than the higher channels among themselves. The time segments shown in Figure 1 include the entire MER data records with a duration of 163.84 s. These time segments do not always cover the entire impulsive flare phase; major parts of the main flare phase are missing in flares 2 and 3, where the preset MER record stops before the HXR peak count rate is reached. The segments used in the TOF analysis are marked with a vertical solid line (begin) and a dashed line (end) in Figure 1, excluding time intervals without significant fine structure or with opposite delay characteristics.

From the detailed analysis of the Masuda flare of 1992 January 13 (Paper III), it became clear that the pulsed fine structure can have a distinctly different timing than the slowly varying HXR flux, differing in sign and magnitude of the energy-dependent time delay. Consequently, we have to examine carefully how these two time structures can be properly separated and how the measured time delays depend on the separation algorithm. We attempt this task with a Fourier filter (briefly called *FFT filter* because we use the fast Fourier transform). We truncate the Fourier power spectrum at a selected cutoff frequency and obtain the time profile of the *pulsed HXR fine structure* F^P from the inverse Fourier transform of a high pass range of the power spectrum. We determine the cutoff frequency for each flare individually using a physical criterion that optimizes the separation between opposite time delay characteristics (see detailed description in § 2.8). We add an additive constant to the filtered HXR flux $F^P(t)$ to render it positive, which has no effect on the time delay measurements (via cross-correlation). The complementary component, the *smooth HXR flux* F^S, is then simply defined by the difference to the total HXR flux F^X, obeying the relation

$$F^X(t) = F^S(t) + F^P(t) . \quad (1)$$

The smooth HXR flux F^S is also shown in Figure 1 (smooth time profiles), overlaid on the (rapidly fluctuating) total HXR flux F^X. The pulsed HXR flux F^P is explicitly shown in Figure 2, summed together from the channels shown in

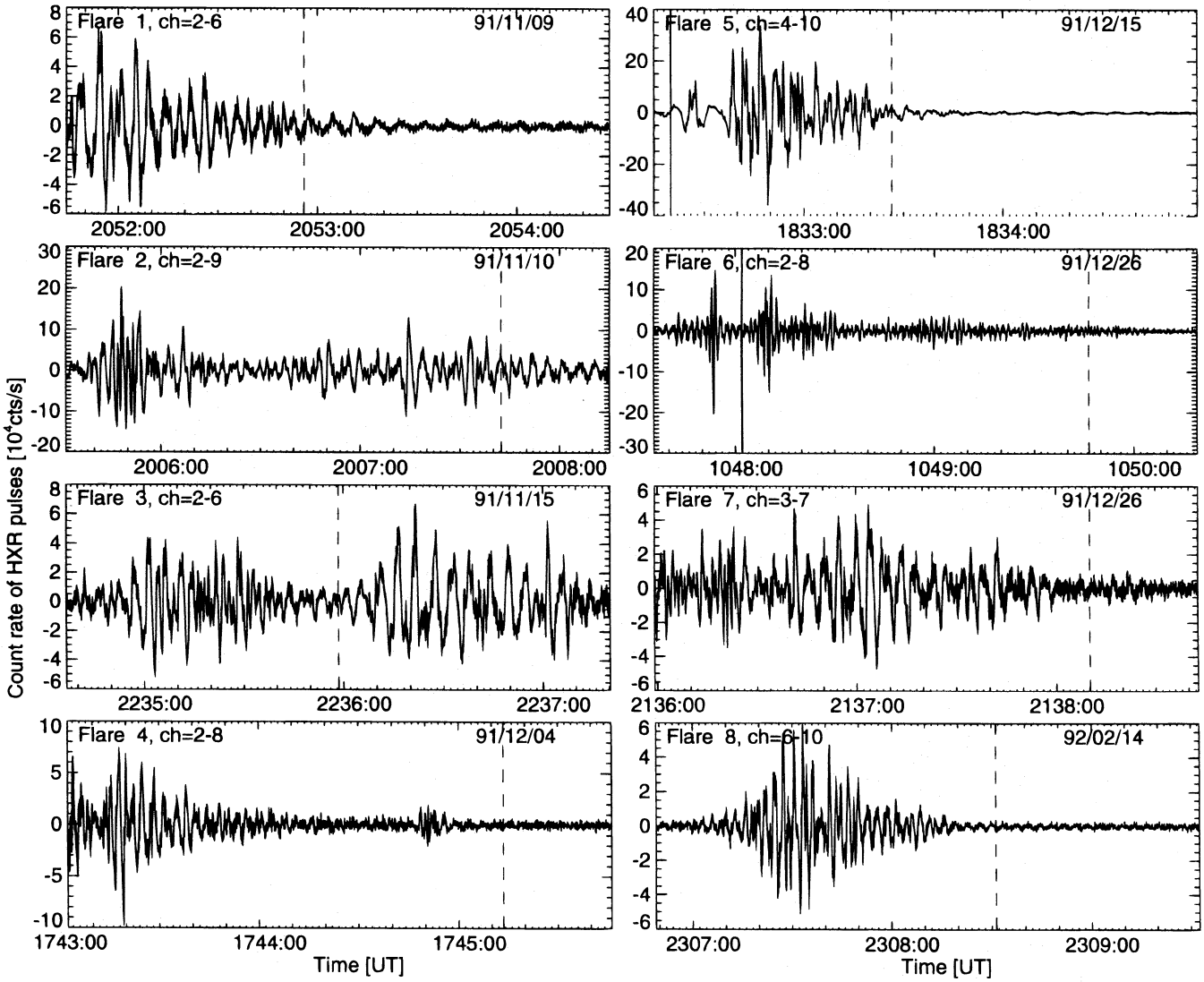

FIG. 2.—HXR fine structure of the analyzed eight flares, obtained by filtering the total HXR flux (integrated over the channels shown in Fig. 1) with a FFT high pass filter. The timescale of the cutoff in the FFT high pass filter is optimized for each flare (see Fig. 8). Note the evolution of quasi-periodic (probably nonlinear) oscillations in the filtered time profiles.

Figure 1. This detrended flux F^P (Fig. 2) shows the time episodes and evolution of rapidly varying fluctuations clearer than the total flux F^X (Fig. 1). The structure of the fine structure F^P can be characterized with groups of quasi-periodic pulses that grow and decay in amplitude almost like a coupled oscillator system that tunes and detunes in and out of resonance. However, there is no strict periodicity in any of these pulse groups, as it is typical for nonlinear dissipative systems. The detailed analysis of these temporal structures in terms of nonlinear dynamics is beyond the scope of this study and will be investigated elsewhere. The most essential point for this study is that all the timing information of electron TOF propagation effects is entirely contained in the pulses of this rapidly varying fine structure F^P (Fig. 2), while the smooth HXR flux F^S lacks completely this information and even exhibits an opposite timing regarding sign and magnitude of the energy-dependent time delay.

2.5. *Autocorrelation Width of HXR Pulses*

One of the simplest ways to characterize the pulses of the HXR fine structure $F^P(t)$ is to examine the autocorrelation function, which is shown in Figure 3, obtained from the same time intervals (indicated with a vertical solid and dashed line in Fig. 2) used in our TOF analysis. We compute the FWHM w_P of the autocorrelated pulses by interpolating their widths at the half-peak amplitude between the base level of the first minimum (indicated with a horizontal dashed line in Fig. 3) and the central maximum at zero time lag. We find pulse widths w_P between 0.4 and 1.6 s (listed in Table 1). If the fine structure would consist of pure random noise, the autocorrelation width would correspond to a δ function with a finite resolution of 64 ms. In the case of a periodic time series the autocorrelation width corresponds to a half-period. We use the autocorrelation width w_P to characterize the typical duration of the pulses.

The autocorrelation width can also be used to distinguish systems with different nonlinear dynamics or to identify evolutionary changes and transitions from one system to another. A most interesting case is flare 3 (91/11/15), which shows two distinctly different episodes regarding time structure. In Figure 4 we show that not only the autocorrelation width differs between two subsequent time segments (before and after 2236:00 UT), but also the time delay character-

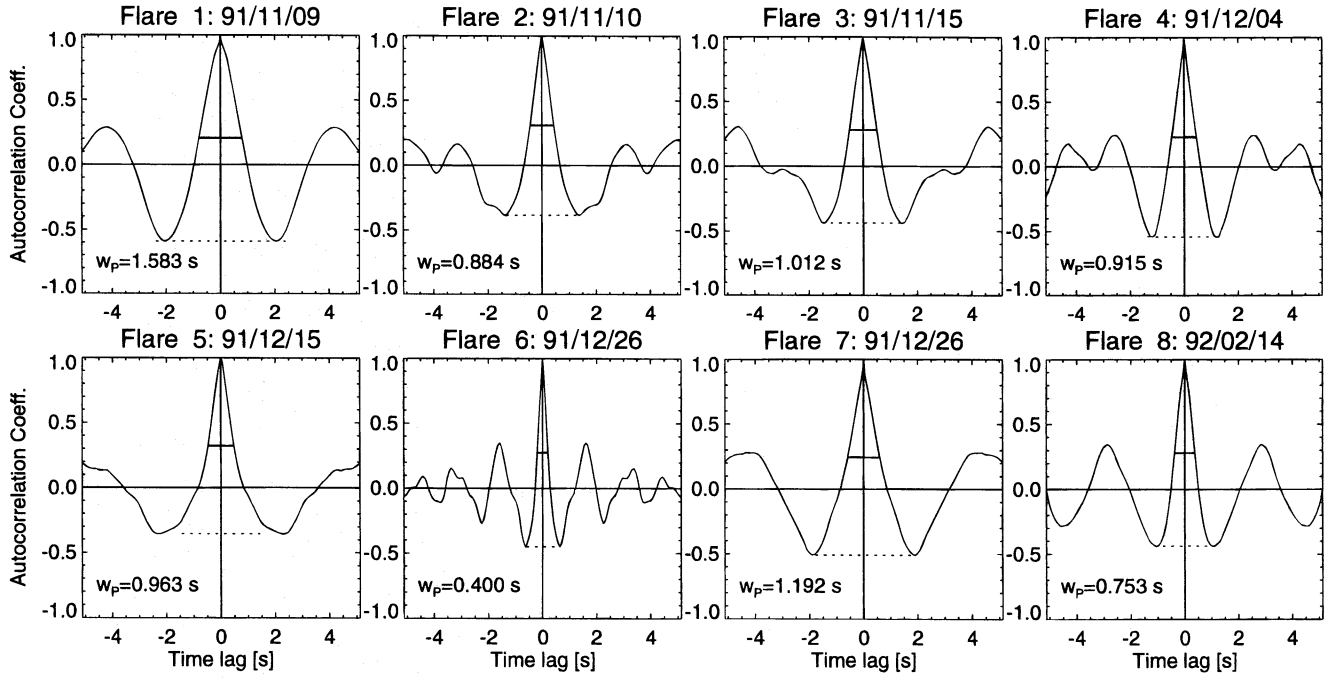

FIG. 3.—Autocorrelation function of the analyzed time segments of the eight flares shown in Fig. 2. The width of the autocorrelation function w_P is determined from the FWHM of the central peak above the base level defined by the first minimum (*dashed line*) of the autocorrelation function. The width w_P is a measure of the characteristic timescale of the filtered HXR pulses.

istics are opposite. The time delay of low-energy electrons is positive during the first segment (Fig. 4, *bottom left*), but negative during the second segment (Fig. 4, *bottom right*). Consequently, we can only use the first segment for our TOF analysis. The transition from a positive to a negative HXR time delay indicates a change from directly precipitating electrons to trapped electrons, possibly related to different loop structures. Indeed, other studies with imaging data show an evolution with multiple loop structures (see § 3.3, and references therein).

2.6. *Time Delay Measurements of HXR Pulses*

We measure now time delays τ_{ij} of the HXR pulse time profiles $F_i^P(t)$ between different energy channels i and j. The time delays are measured with the cross-correlation technique as described and examined in Paper II, optimized for suppressing aliasing effects and incomplete time segments. Since most of the TOF-related time delays are smaller than the instrumental resolution of 64 ms, an interpolation scheme is used to determine the accurate value of the time delay defined by the peak of the cross-correlation coefficient. The uncertainties σ_τ of the measured time delays are determined by repeating the delay measurements 100 times with added Poisson noise $F_i^P(t) + \rho(t)[F_i^X(t)]^{1/2}$ [with $\rho(t)$ positive and negative random numbers with a standard deviation of unity], according to the method described in Paper II.

The time delay measurements τ_{ij} of all eight analyzed flares are presented in Figure 5 and the numeric values are listed in Table 2. The reference channel i is always the lowest energy channel, because of the highest signal-to-noise ratio, while the second cross-correlated channel $j = i + 1, \ldots, j_N$ steps through all higher channels. (The channel ranges are indicated in Fig. 1 or in Tables 1 and 2). We were able to perform independent time delay measurements between 7 channel pairs (in one flare), 6 channel pairs (in three flares), and 4 channel pairs (in four flares), although the pulsed HXR flux F_P represents only a few percent of the total HXR flux F_X. This unprecedented energy coverage of time delay measurements allows us to test in detail the functional shape of theoretical timing models.

We show in Figure 5 fits of a one-parameter model that describes the electron TOF differences over a distance l, assuming simultaneous electron injection at the start and simultaneous energy loss at the end of the distance l. This model, briefly called the *TOF model*, is also described in Papers I–V and we repeat here only the essential definitions. Electron TOF differences can be expressed in terms of velocity differences,

$$\tau_{ij} = \frac{l}{c}\left(\frac{1}{\beta_i} - \frac{1}{\beta_j}\right), \tag{2}$$

where the electron velocities $v_i = c\beta_i$ are defined by the relativistic kinetic electron energies $E_i = m_e c^2(\gamma_i - 1)$ and the Lorentz factor $\gamma_i = (1 - \beta_i^2)^{-1/2}$,

$$v(E) = c\sqrt{1 - \left(1 + \frac{E}{m_e c^2}\right)^{-2}}. \tag{3}$$

The relation between electron energies E_i and HXR photon energies ε_i involves the convolution with the bremsstrahlung cross section $\sigma(\epsilon, E)$ and was simulated in Paper IV for time-dependent electron injection spectra (characterized by a power-law spectrum with slope δ and high-energy cutoff E_0) in terms of the thick-target model ($\delta = \gamma + 1$; Brown 1971). We use these conversion factors $q_E(\epsilon, \gamma, E_0)$ computed according to Paper IV (listed in Table 2) to retrieve the timing $E(t)$ of electrons by converting the timing $\epsilon(t)$ of HXR photons:

$$E(t) = \epsilon(t) q_E(\epsilon, \gamma, E_0). \tag{4}$$

Previously, we had fitted the HXR spectra with a single

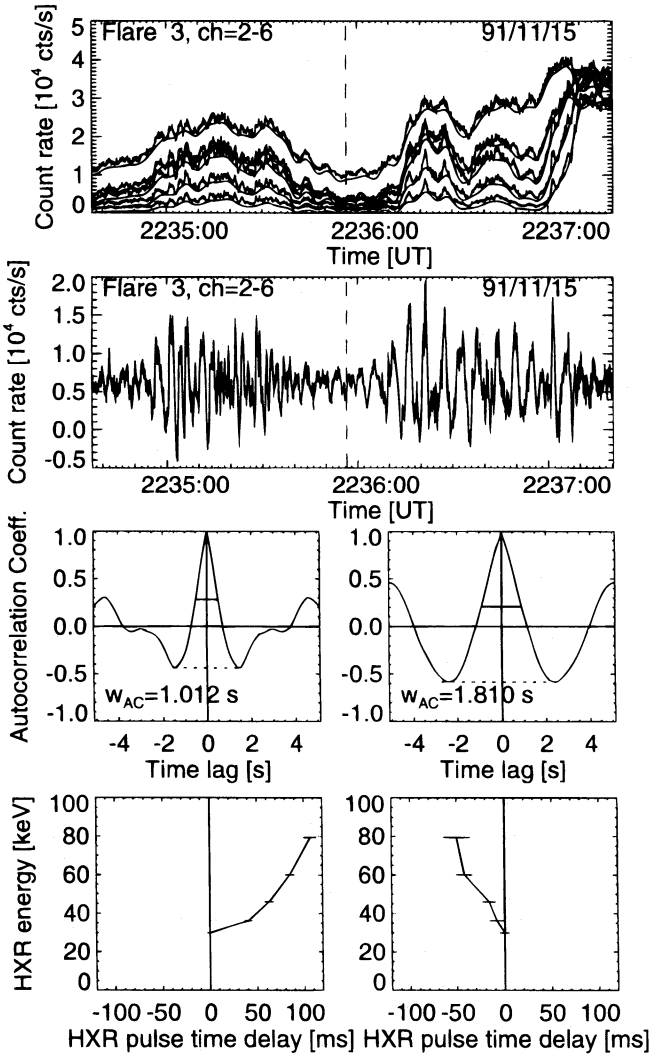

FIG. 4.—Example of a flare (no. 3, 91/11/15) with two episodes of distinctly different time characteristics, changing from positive to negative time delays [$\tau_{ij} = t(E_i) - t(E_j)$, $i = j_{\min}$] for the filtered HXR pulses. *Top:* time profiles of channels 2–6, with the two time segments separated by a dashed vertical line; *Second row:* HXR pulses filtered with a FFT high pass filter and a cutoff timescale of $t_F = 3.0$ s; *Third row:* autocorrelation function of the two time segments; *Bottom row:* time delay τ_{ij} of HXR pulses measured between the energy channels $i = 2$ and $j = 3$–6. The uncertainties of the time delays caused by Poisson noise are indicated with horizontal error bars.

power law in the relevant time ranges used in the TOF analysis. The power-law spectral indices γ (with values in the range of 2.75 to 4.12) are listed in Table 1. Because we did not detect obvious high-energy drop-offs in the HXR spectra of these eight flares, we adopted the highest value $E_0 = 10$ MeV (used in the simulations in Paper IV) for the high-energy cutoff of the electron injection spectra. The HXR photon energies ϵ for each channel were computed from the medians of the channel count spectra $R_i(\epsilon)\epsilon^{-\gamma}$, using the MER detector response functions $R_i(\epsilon)$ as described in Paper IV.

The procedure described above is used to fit the measured time delays τ_{ij} and yields the electron TOF distance l. This length l of the electron orbit trajectory, however, cannot directly be compared with loop geometries, because the electron flight path is also subject to the electron Larmor motion and helical twist of magnetic field lines. These effects have been studied in Paper III, where a factor of $q_\alpha = 0.64$ was inferred for the pitch-angle correction and a factor of $q_H \approx 0.85$ for the helicity correction, yielding a *projected TOF distance* l',

$$l' = l\, q_\alpha q_H \approx l 0.54 \,. \quad (5)$$

The *projected TOF distance* l' represents the length of the central axis of helically twisted magnetic lines, which in turn constitute the guiding center of the Larmor motion of the electrons. Thus, the *projected TOF distance* l' represents the relevant length parameter to be compared with flare loop geometries.

The fits of the TOF model shown in Figure 5 clearly demonstrate that our simple one-parameter is fully consistent with the data over the entire energy range (up to $\lesssim$300 keV) within the uncertainties of the delay measurements. We compute also the reduced χ^2 values of the best fits (indicated at the tops of each panel in Fig. 5) and find a satisfactory fit quality with $\chi^2 \lesssim 1.0$ in all flares. Thus, the TOF model provides surprisingly good fits to all pulsed HXR fine structure (with positive delays at lower energies) for all flares without failing in a single case. Therefore, we see no reason to include additional timing effects such as acceleration or energy-loss timescales for these cases. The inferred projected TOF distances l' range from 14,000 $\pm$ 2000 km (flare 6) to 30,000 $\pm$ 8000 km (flare 7). The average uncertainty (the formal error of the χ^2 fit) ranges from $\sigma_{l'}/l' = 6\%$ to 26%. Note that the value of these uncertainties, varying in the range of $\sigma_{l'} = 1300$–7700 km, is comparable with the resolution of *Yohkoh* SXT images (2.″46 $\approx$ 1700 km).

2.7. *Time Delay Measurements of the Smooth HXR Flux*

Since we are primarily interested in the determination of electron TOF distances, for which only the HXR fine structure is relevant, we do not model the delay characteristics of the smooth HXR flux in this study but focus only on the aspects that are important for its discrimination from the fine structure.

The energy-dependent time delays of the smooth HXR flux F_S are shown in Figure 6 (*thick lines*), together with the delays of the pulsed HXR fine structure (*dashed lines*). We note that in all cases, except for one (flare 7), the delays of the smooth HXR flux become more negative with increasing energy, probably because of collisional energy loss in the corona or collisional deflection in a trap with subsequent precipitation (Paper II). In flare 7, as well as in other cases (flares 2 and 4) at low energies, the delay is positive, probably indicating a convolution with thermal effects, that delay the peak of thermal HXRs (at low energies) with respect to the nonthermal HXRs (at higher energies), similar to the Neupert effect (Dennis & Zarro 1993).

In all eight flares, the delays of the smooth HXR flux are always larger ($\approx$1 s) in magnitude (regardless of the sign) than the tiny delays ($\approx$100 ms) of the HXR fine structure. Thus, an incorrect separation of the fine structure from the smooth flux will result in a contaminated delay measurement for the fine structure. We illustrate this contamination effect schematically in Figure 7. Let us assume that the fine-structure flux F_P and the smooth HXR flux F_S are produced by electrons with physically distinct timing characteristics, and that the two components can be properly separated with a FFT filter timescale t_F. If we erroneously use too large a filter timescale t_F, an admixture of the

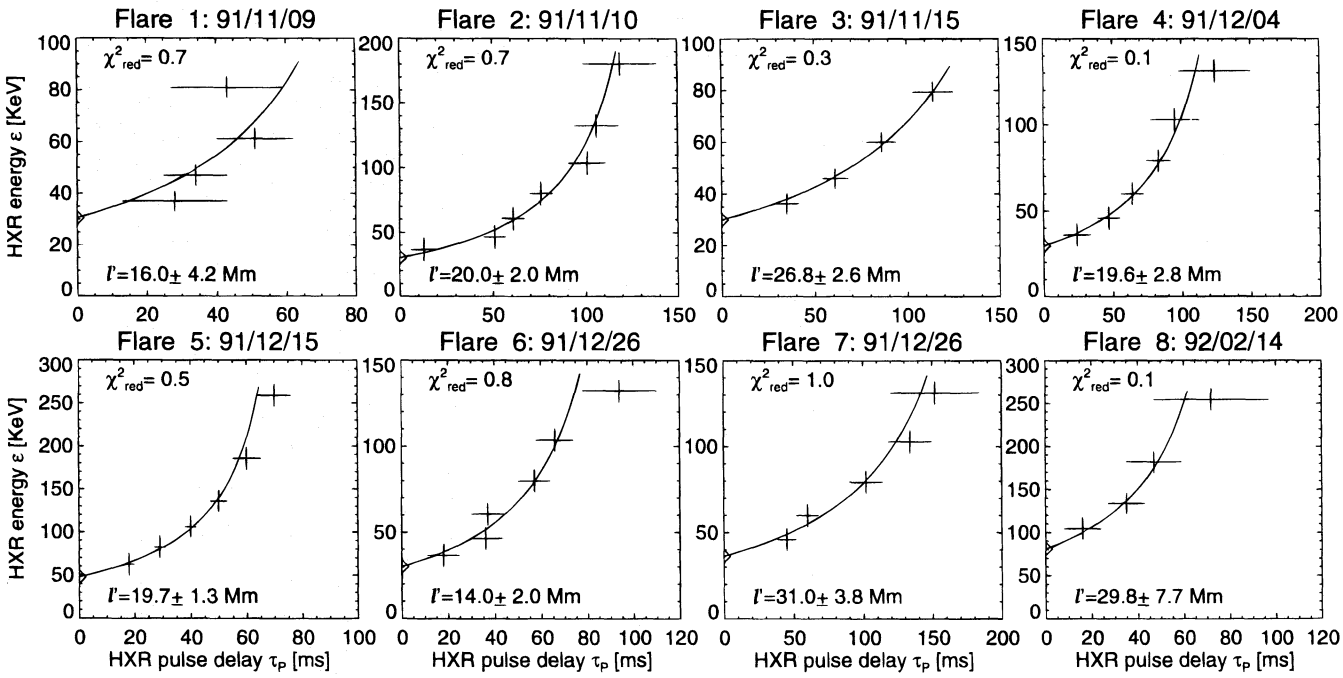

FIG. 5.—Energy-dependent time delays $\tau_{ij} = t(E_i) - t(E_j)$ of the filtered HXR pulses $F^P(t)$ shown in Fig. 2, measured from cross-correlation between the energy channels E_i and E_j (with $i = j_{\min}$) during the selected time segments shown in Fig. 1. The horizontal bars represent the uncertainties of the delay measurements caused by Poisson noise (the vertical bars are arbitrary). The curve represents the best fit of the TOF model $\tau_{ij} = (l/c) * (1/\beta_i - 1/\beta_j)$. The projected TOF distance $l' = l * 0.54$ and the $\chi^2_{\rm red}$ of the best fit is indicated in each panel.

smooth HXR flux is contained in the cross-correlated fine structure, and the resulting time delay will be smaller than the correct value if the smooth HXR flux has an opposite timing (Fig. 7, *top panels*), or larger if the smooth HXR flux has a larger delay of equal sign (Fig. 7, *bottom*). On the other side, if too small a FFT filter time constant is chosen, the smooth HXR flux F_S has no side effect on the resulting delay, but substructures of the HXR pulses may have variable timing characteristics.

2.8. *Timescale Filter*

In order to investigate the filter effects on the delay measurements systematically we perform time delay measurements τ_{ij} of the pulsed HXR fine structure F_P for all flares

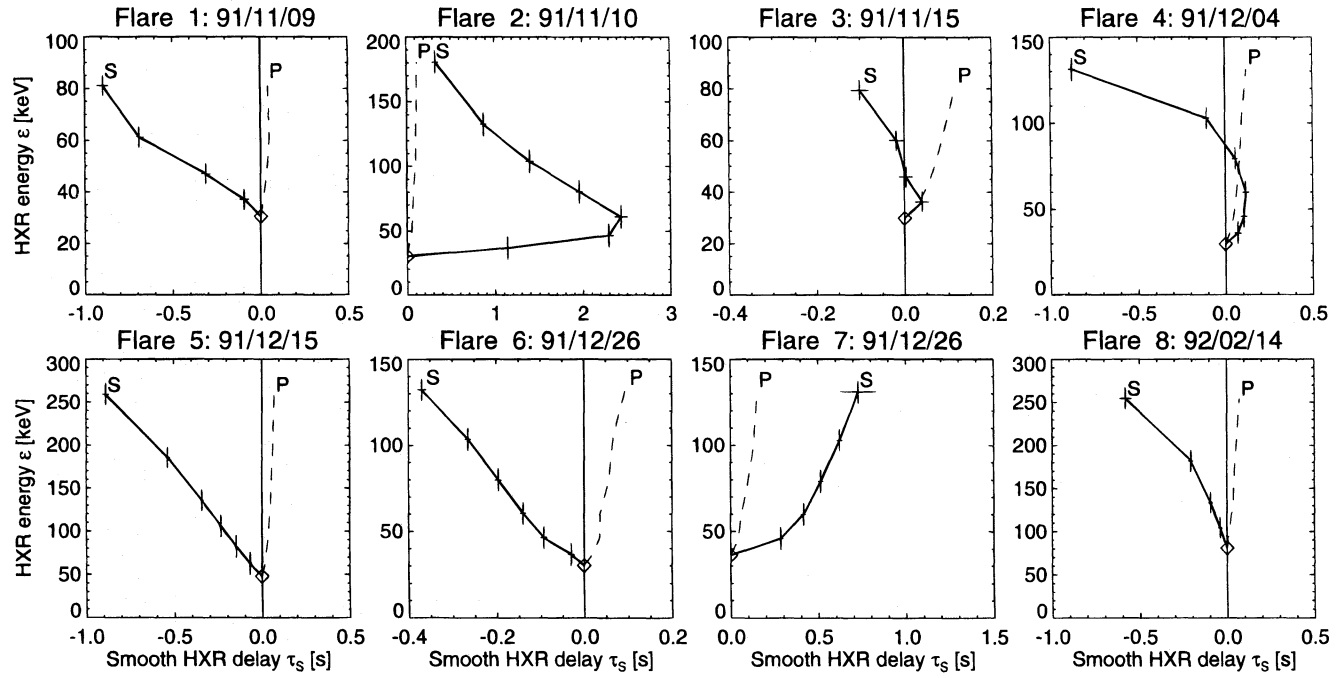

FIG. 6.—Energy-dependent time delays τ_{ij} of the smoothly varying HXR flux $F_S(t)$, measured from the same energy channels and time segments as shown in Fig. 1. The horizontal bars represent the uncertainties of the delay measurements based on Poisson statistics. The delay of the pulsed HXR flux $F_P(t)$ is also shown for comparison (*dashed line*).

TABLE 2

ENERGY-DEPENDENT HXR TIME DELAYS AND ELECTRON PROPAGATION TIMES

Flare Number	Channel[a] j	Photon Energy[b] ϵ_j (keV)	Conversion Factor[c] q_{E_j}	Electron Energy[d] E_j (keV)	CCC[e]	Time Delay[f] τ_{ij} (ms)	TOF Difference[g] $\Delta t_{ij}^{\rm prop}$ (ms)	Propagation Time[h] $t_j^{\rm prop}$ (ms)	TOF Distance[i] l' (Mm)
1.....	2	30.5	2.403	73.3	1.000	0 ± 0	0	202	16.0 ± 4.2
	3	37.1	2.394	88.8	0.692	28 ± 15	14	187	...
	4	47.0	2.383	112.0	0.679	34 ± 9	30	171	...
	5	61.3	2.372	145.4	0.598	51 ± 11	45	156	...
	6	81.0	2.352	190.5	0.471	43 ± 16	59	143	...
2.....	2	30.2	2.152	65.0	1.000	0 ± 0	0	265	20.0 ± 2.0
	3	36.7	2.147	78.8	0.537	13 ± 7	20	245	...
	4	46.5	2.140	99.5	0.528	51 ± 6	41	223	...
	5	60.7	2.132	129.4	0.460	61 ± 6	62	203	...
	6	80.2	2.121	170.1	0.398	76 ± 6	80	185	...
	7	103.8	2.108	218.8	0.306	101 ± 10	93	171	...
	8	132.6	2.094	277.6	0.275	106 ± 12	104	160	...
	9	180.5	2.073	374.2	0.188	119 ± 20	115	150	...
3.....	2	29.9	1.990	59.5	1.000	0 ± 0	0	369	26.8 ± 2.6
	3	36.3	1.989	72.2	0.512	35 ± 7	28	340	...
	4	46.0	1.985	91.3	0.559	61 ± 7	59	310	...
	5	60.1	1.977	118.8	0.499	86 ± 8	88	280	...
	6	79.4	1.970	156.4	0.426	114 ± 11	114	255	...
4.....	2	29.8	1.963	58.5	1.000	0 ± 0	0	272	19.6 ± 2.8
	3	36.2	1.961	71.0	0.503	24 ± 10	21	250	...
	4	45.9	1.956	89.8	0.530	47 ± 8	43	228	...
	5	60.0	1.948	116.9	0.472	64 ± 8	65	206	...
	6	79.3	1.941	153.9	0.433	83 ± 9	84	187	...
	7	102.9	1.932	198.8	0.308	95 ± 18	99	173	...
	8	131.2	1.922	252.2	0.171	124 ± 26	110	161	...
5.....	4	47.7	2.805	133.8	1.000	0 ± 0	0	197	19.7 ± 1.3
	5	62.2	2.778	172.8	0.930	18 ± 2	16	181	...
	6	82.1	2.745	225.4	0.855	29 ± 2	30	167	...
	7	105.9	2.713	287.3	0.748	40 ± 2	40	157	...
	8	135.8	2.674	363.1	0.650	50 ± 3	49	148	...
	9	185.5	2.621	486.2	0.536	60 ± 5	57	140	...
	10	259.0	2.555	661.8	0.428	70 ± 6	63	134	...
6.....	2	30.1	2.096	63.1	1.000	0 ± 0	0	188	14.0 ± 2.0
	3	36.5	2.096	76.5	0.492	18 ± 7	14	173	...
	4	46.3	2.089	96.7	0.507	36 ± 7	29	158	...
	5	60.5	2.079	125.8	0.471	37 ± 7	44	143	...
	6	79.9	2.070	165.4	0.388	57 ± 7	57	130	...
	7	103.5	2.059	213.1	0.306	66 ± 8	67	121	...
	8	132.2	2.045	270.4	0.226	94 ± 16	74	113	...
7.....	3	36.2	1.945	70.4	1.000	0 ± 0	0	398	31.0 ± 3.8
	4	45.9	1.939	89.0	0.540	45 ± 7	35	362	...
	5	59.9	1.935	115.9	0.535	60 ± 8	70	327	...
	6	79.2	1.927	152.6	0.457	102 ± 12	100	297	...
	7	102.8	1.918	197.2	0.370	134 ± 16	123	274	...
	8	131.1	1.908	250.2	0.271	152 ± 32	141	256	...
8.....	6	80.8	2.309	186.6	1.000	0 ± 0	0	268	29.8 ± 7.7
	7	104.5	2.291	239.4	0.550	16 ± 8	18	249	...
	8	133.6	2.272	303.5	0.478	35 ± 8	33	234	...
	9	182.1	2.243	408.4	0.317	47 ± 12	48	219	...
	10	254.6	2.203	561.0	0.176	72 ± 25	60	207	...

[a] Channel j is cross-correlated with channel $i = j_{\rm min}$.
[b] ϵ_j is median of count spectrum $C(\epsilon) = R_j(\epsilon)\epsilon^{-\gamma}$.
[c] Conversion factor $q_E(\epsilon_j, \gamma, E_0 = 10$ MeV).
[d] Electron energy $E_j = q_E\epsilon_j$.
[e] Cross-correlation coefficient between channel i and j.
[f] Measured HXR time delay $\tau_{ij} = t(E_i) - t(E_j)$ with uncertainty $\sigma_{\tau_{ij}}$.
[g] Electron TOF difference based on fitted model $\Delta t_{ij}^{\rm prop} = t^{\rm prop}(E_i) - t^{\rm prop}(E_j)$.
[h] Electron TOF propagation time based on fitted model $t^{\rm prop}(E_j) = l/v(E_j)$.
[i] Projected TOF distance $l' = lq_\alpha q_H \approx l0.54$.

over an extended range of filter timescales, i.e., 0.5 s $\leq t_F \leq$ 6.0 s in steps of 0.5 s (or smaller in some cases). In Figure 8 we show for each flare how the (projected) TOF distance l' fitted to the time delays of the filtered HXR fine structure F_P varies as function of the filter timescale t_F. Each data point with an error bar in Figure 8 represents a least-χ^2 fit as shown in Figure 5. Only the results of filter timescales t_F with acceptable fits for l' are shown, either with a satisfactory $\chi^2_{\rm red} \lesssim 1$ or with small deviations $|\tau_{ij}^{\rm obs} - \tau_{ij}^{\rm model}| \lesssim 10$ ms.

First, we note that the range of filter timescales t_F leading to satisfactory fits of the TOF model varies from flare to flare, and that the obtained best fit for the TOF distance l' varies generally as function of the filter timescale. Only in

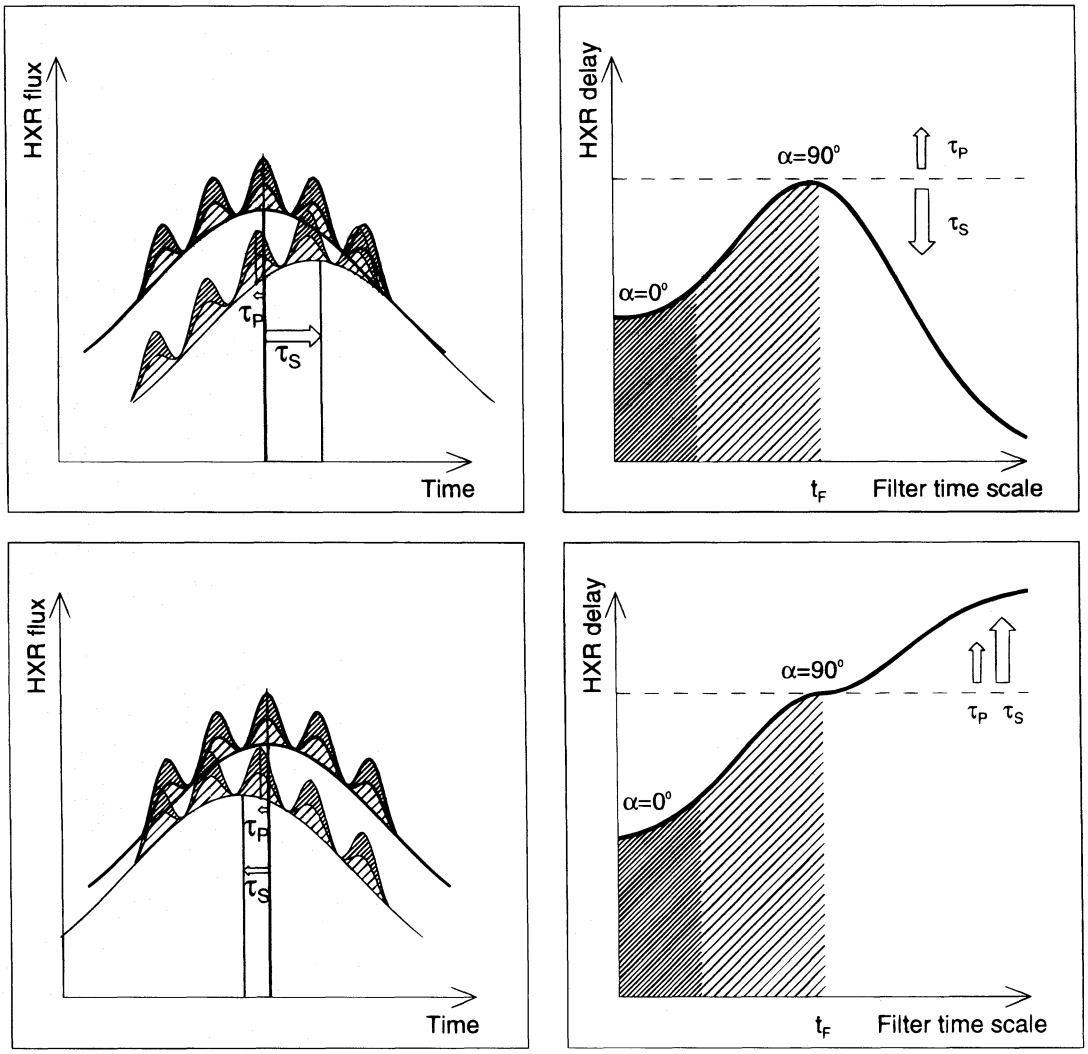

FIG. 7.—The effect of competing time delays between the pulsed and the smoothly varying HXR flux is illustrated for timescale filtered time delay measurements. The time delay (τ_P) of the pulsed HXR flux (*hatched*) and the time delay (τ_S) of the smooth HXR flux (*not hatched*) are opposite in the first case (*top left*), but of the same sign in the second case (*bottom left*). The time delay of the HXR pulses is most accurately measured at a filter timescale of t_F, where both components are exactly separated. At longer filter timescales the measured delay is smaller (first case) or larger (second case), depending whether the delays of the two components compete or cooperate. At smaller filter timescales (*double-hatched*), the measured time delay refers only to the peaks of the pulses, which may be associated with electrons of different timing conditions (e.g., due to different pitch angles, indicated with $\alpha = 0°$ and $\alpha = 90°$ in the right panels).

flare 3 do we find that the inferred TOF distance is constant within $\lesssim 10\%$ over a large filter range (of $t_F = 1.5$–6.0 s). In order to understand the variation in the other cases we consult Figure 7. Most of the flares show a pronounced peak of the TOF distance l' versus the filter timescale t_F, similar to the first case in Figure 7 (*top*), where the delay of the smooth HXR flux is opposite to the delay of the fine structure, and thus responsible for the underestimation of the TOF distance l' at larger filter timescales. In flare 4, we see the opposite case, where the fitted TOF distance increases for timescales $t_F \geq 2.5$ s, similar to the second case shown in Figure 7 (*bottom*), where the smooth HXR flux and the HXR fine structure have the same sign of the delay. Thus, the variation of the fitted TOF distance at large filter timescales t_F can be understood in terms of contaminations from competing time delays of the smooth HXR flux (see Fig. 6).

At shorter filter timescales than t_F we find that the fitted TOF distance l' always decreases. This must be caused by a physical reason other than competing time delays from the smooth HXR flux. For a given flare with a well-defined separation between the acceleration site and the energy-loss site at the chromospheric footpoints (in terms of the thick-target model), the variation of the electron TOF distance is probably caused by different pitch angles or helical twist. In a model in Paper III, we estimated that the two effects cause a correction factor of $q_\alpha q_H = 0.54$ for electrons that arrive with a perpendicular pitch angle at the chromosphere. For some flares (2 and 5), where the TOF distance could be fitted over a large range of filter timescales down to the shortest scales of $t_F = 0.5$ s (in Fig. 8), the inferred TOF distance is indeed about a factor 0.5 shorter than at the maximum. Also, it is likely that the fastest timescales are conserved by those electrons with the smallest pitch angles, because they suffer the least time smearing by multiple paths or by pitch-angle scattering. Based on these two arguments, we propose the interpretation that the shorter TOF distances measured with the fastest time filters are associated with electrons with nearly parallel pitch angles (indicated with $\alpha = 0$ and double-hatched regimes in Fig. 7),

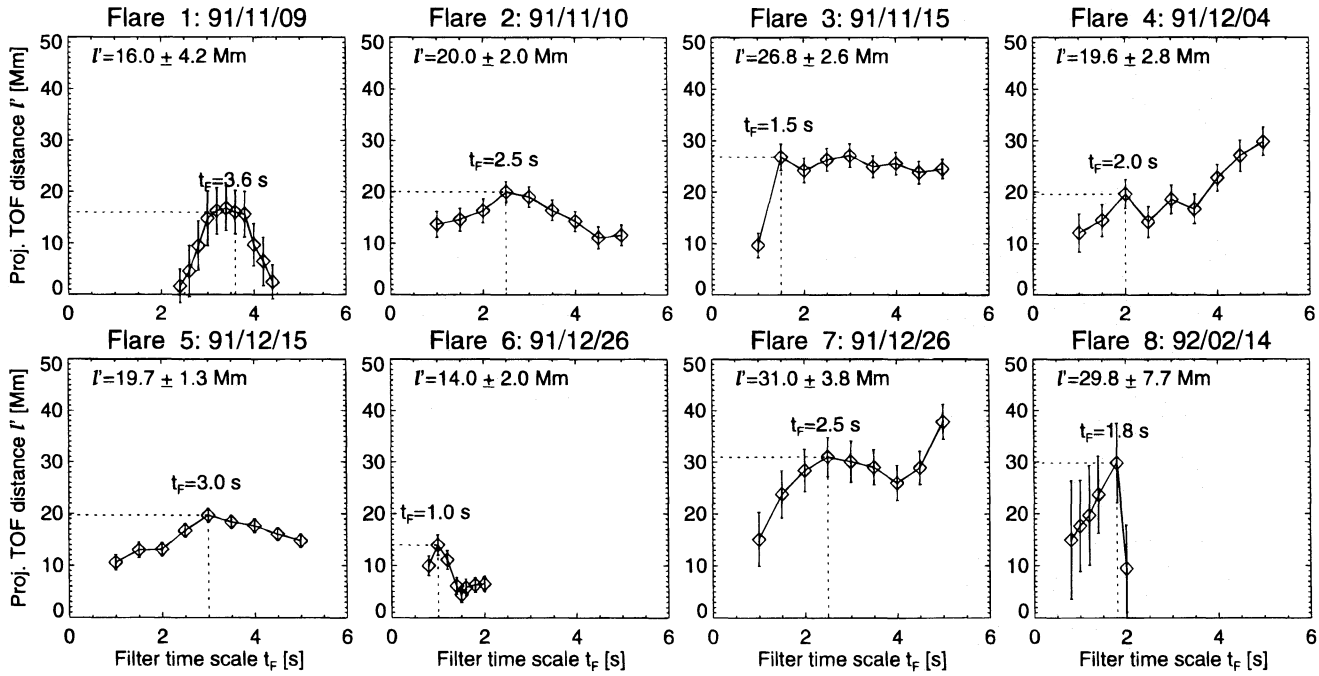

FIG. 8.—Measurements of projected TOF distances l' vs. the timescale t_F of the FFT filter, which is used to separate the HXR pulses from the smoothly varying HXR flux for the eight flares listed in Table 1. The data points (*diamonds*) are shown for those values of filter timescales t_F for which an acceptable fit of the TOF model $t^{\rm prop}(E) = l/v(E)$ was obtained. The dashed lines and the corresponding values of l' and t_F mark the first peak or plateau of the function $l'(t_F)$ encountered at small timescales t_F.

while the longer TOF distances measured from HXR fine structure using larger time filters (but not contaminated by competing time delays from the smooth HXR flux) are associated with electrons of nearly perpendicular pitch angles at the precipitation site (indicated with $\alpha = 90°$ and single-hatched regimes in Fig. 7). Following this interpretation, we identify the relevant filter timescale t_F with the maximum value of the function $l'(t_F)$ in the case of a single maximum (flares 1–3, 5–8), or with the first maximum or plateau at the side of short filter timescales in other cases (flare 4). The so-identified filter timescales t_F are marked with dashed lines in Figure 8 (and listed in Table 1), defining the relevant TOF distances l' associated with electrons of nearly perpendicular pitch angles at the precipitation site. For isotropic electron acceleration or injection, the pitch angle distribution at the precipitation site always contains more electrons with large pitch angles than with small ones [because of $df(\alpha) \propto \sin \alpha \, d\alpha$ and the conservation of the magnetic moment], and thus, electrons with large pitch angles will dominate the HXR pulses generated at the chromospheric thick-target HXR emission site.

2.9. *Correlation of TOF Distance and Pulse Width*

After we have inferred electron TOF distances, which supposedly represent a measure of the spatial separation between the acceleration site and the chromospheric footpoints of the flare loops, we wonder whether the duration of the HXR pulses that carry all the TOF timing information are somehow related to the length of the TOF path. In Figure 9 we show scatter plots between three parameters: the filter timescale t_F, the pulse width w_P (determined from the autocorrelation), and the TOF distance l'. The pulse widths w_P scatter around the values $t_F/2$, as expected for a quasi-periodic sequence of pulses (Fig. 9, *left*). The projected

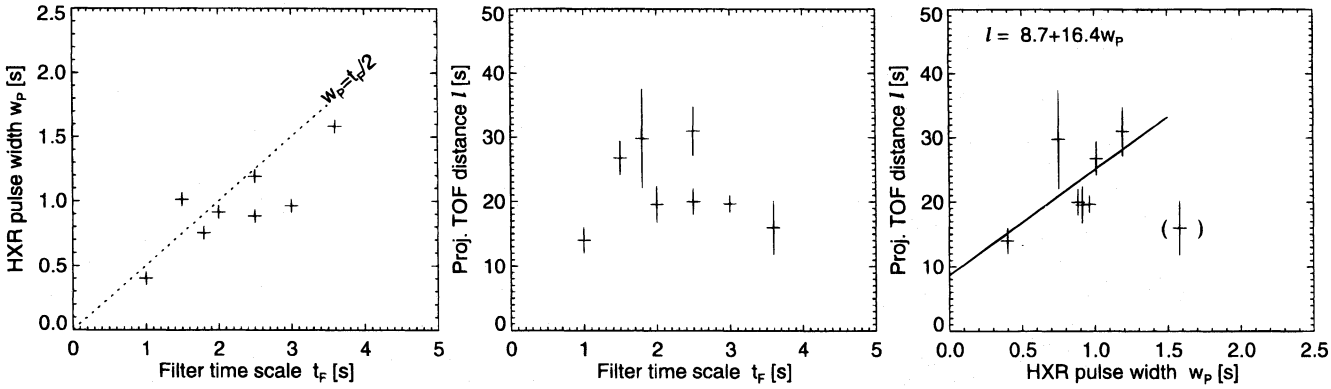

FIG. 9.—Correlations between the HXR pulse width w_P, the filter timescale t_F, and the (projected) electron TOF distance l' for the eight analyzed flares. The lines represent the relation $w_P = t_F/2$ (*left panel*) and a linear regression fit (*right panel*), excluding one flare (+) with two competing timescales.

TOF distances l' do not show an obvious correlation to the filter timescale t_F (Fig. 9, *middle*), and are therefore not dominated by possible artifacts of our filter method. However, we find the possibility of a correlation between the TOF distance l' and the pulse width w_P, following the linear relation $l' = 9 + 16w_P$ (Fig. 9, *right*). Although we deal here with small number statistics, it is conceivable that this correlation indicates a physical relation. If the pulses were generated by an Alfvénic disturbance in a flux tube, the pulse width is in some way related to the geometric cross section or length of the flux tube and could explain the correlation between the pulse duration w_P and the flux tube length l' observed here. We will investigate and model this relation in more detail at a later stage, when more statistics is available.

3. *YOHKOH* DATA ANALYSIS

3.1. *The Yohkoh HXT and SXT Instruments*

The Hard X-Ray Telescope (HXT) on board the *Yohkoh* spacecraft has been operational since 1991 October. HXT is a hard X-ray imager of the Fourier synthesis type with 64 modulation subcollimators, each measuring the spatially modulated incident photon counts. Four images are simultaneously taken in the four energy channels: Lo band (14–23 keV), M1 band (23–33 keV), M2 band (33–53 keV), and Hi band (53–93 keV). The imager has a wide field covering the whole Sun. The finest width of the collimators is $\approx 8''$ (≈ 6000 km). The sensitive area is ≈ 70 cm^2. Instrumental descriptions of HXT can be found in Kosugi et al. (1991). The basic time resolution is 0.5 s, but we synthesized images over durations of 22–87 s (Table 3), over time intervals that closely coincide with the *CGRO* TOF measurements. We used the standard *maximum entropy method* for the image reconstruction (task HXT-MULTIMG developed by T. Sakao and J. McTiernan).

Soft X-ray images are taken simultaneously with the Soft X-Ray Telescope (SXT) on board *Yohkoh* with an enhanced cadence during the flare mode. SXT is a grazing-incidence telescope recording with a CCD camera with 1024 × 1024 pixels and a pixel size of 2.″46. For technical descriptions see Tsuneta et al. (1991). We produced coregistered overlays of SXT and HXT images using the standard pointing data from the spacecraft attitude files. The accuracy of the coregistration seems to be within ≈ 1 SXT pixel (2.″46) in all cases. We selected SXT images simultaneously during the time segments analyzed from *CGRO*, except when SXT entered late into flare mode (after the *CGRO* burst trigger).

3.2. *Loop Geometries and Projection of TOF Distances*

The TOF distances l' measured with *CGRO* are spatially projected onto flare loops observed in simultaneous *Yohkoh* images (Fig. 10). The frames shown in Figure 10 consist of two overlays of various HXT and/or SXT images (Fig. 10, *left and middle columns*) and a projection of the vertical plane (Fig. 10, *right column*), for each of the eight analyzed flares. Our strategy is to identify the position of two footpoints, which define the baseline of a semicircular loop geometry. The assumption of a semicircular loop geometry is mainly based on the appearance of flare loops observed near the limb (e.g., Masuda 1994). Because the size of such a model loop is entirely determined by the footpoint separation, the inclination angle of the loop plane is not critical, and thus we project always into the vertical plane. For an arbitrary line of sight, the projected loop appears as an ellipse centered at the midpoint between the two footpoints. The identification of double footpoints is obvious in most of the flares (1–5, 8). In the other flares (6–7) we use additional information from the elongated lowest HXT contours and the coregistered loop structures seen in SXT.

In each of the projections, we show three geometric elements: the semicircle of the loop (thin circles in Fig. 10), the vertical through the midpoint between the two footpoints (Fig. 10, *thin lines*), and a magnetic field line that has the same length as the *projected TOF distance* l', connecting the footpoints with the vertical in the cusp region (Fig. 10, *thick curves*). The geometry of this magnetic field line is simply composed of two circular segments, with the lower segment having the same radius r as the loop and the upper segment with a radius constrained by tangential connections at the semicircular loop and the vertical. The definition of this cusp field line is the same as in Paper III, with the length l' being related to the loop radius r and the height h of the cusp by

$$l' = \frac{r}{2}\left(1 + \frac{h^2}{r^2}\right) \operatorname{atan}\left(\frac{2hr}{h^2 - r^2}\right). \quad (6)$$

The height h demarcates the centroid position of the hypothetical acceleration region, if electrons are assumed to

TABLE 3

Yohkoh HXT AND SXT PARAMETERS OF EIGHT ANALYZED FLARES

Flare Number	Date	Start HXT (UT)	Duration HXT (s)	HXT Counts (Lo/M1/M2/Hi) (counts s^{-1} SC^{-1})	Location HXT	Loop Radius r (Mm)	TOF Height h (Mm)	Height Ratio h/r	Length Ratio $l'/(r\pi/2)$	SXT PE[a]	SXT IF[b]	References
1.....	91/11/09	2052:03	22	93/105/80/54	S16W67	6.5	14.1 ± 3.7	2.17	1.57	Y	N	1
2.....	91/11/10	2005:32	67	413/181/134/101	S13E45	12.7	12.9 ± 1.3	1.02	1.00	N	Y	1, 12, 15
3.....	91/11/15	2234:39	87	1292/731/528/341	S13W19	13.5	21.5 ± 2.1	1.59	1.26	Y	Y	1–12
4.....	91/12/04	1743:10	26	89/70/36/20	N18E58	10.7	14.9 ± 2.1	1.39	1.16	N	Y	1
5.....	91/12/15	1832:33	30	162/157/152/137	S08E77	8.6	17.0 ± 1.1	1.98	1.46	...	...	1, 13
6.....	91/12/26	1048:02	31	359/89/59/35	N39W16	5.6	12.4 ± 1.8	2.22	1.60	...	...	...
7.....	91/12/26	2136:34	82	164/142/86/42	S16W23	17.0	23.4 ± 2.9	1.38	1.16	Y	Y	1
8.....	92/02/14	2307:20	27	1085/918/514/202	S13E02	12.8	25.8 ± 6.7	2.02	1.49	Y	Y	1,14

[a] SXT PE = plasma ejecta detected by SXT (Y = yes, N = no, ... = no data).

[b] SXT IF = impulsive footpoint brightenings detected by SXT.

REFERENCES.—(1) Sakao 1994; (2) Sakao et al. 1992; (3) Hudson et al. 1992; (4) Canfield et al. 1992; (5) Kane et al. 1993b; (6) Kane et al. 1993a; (7) McTiernan et al. 1994; (8) Kawabata et al. 1994a; (9) Kawabata et al. 1994b; (10) Culhane et al. 1993; (11) Wuelser et al. 1994; (12) Inda-Koide et al. 1995; (13) Aschwanden 1996; (14) Hudson et al. 1994; (15) Yoshimori et al. 1992

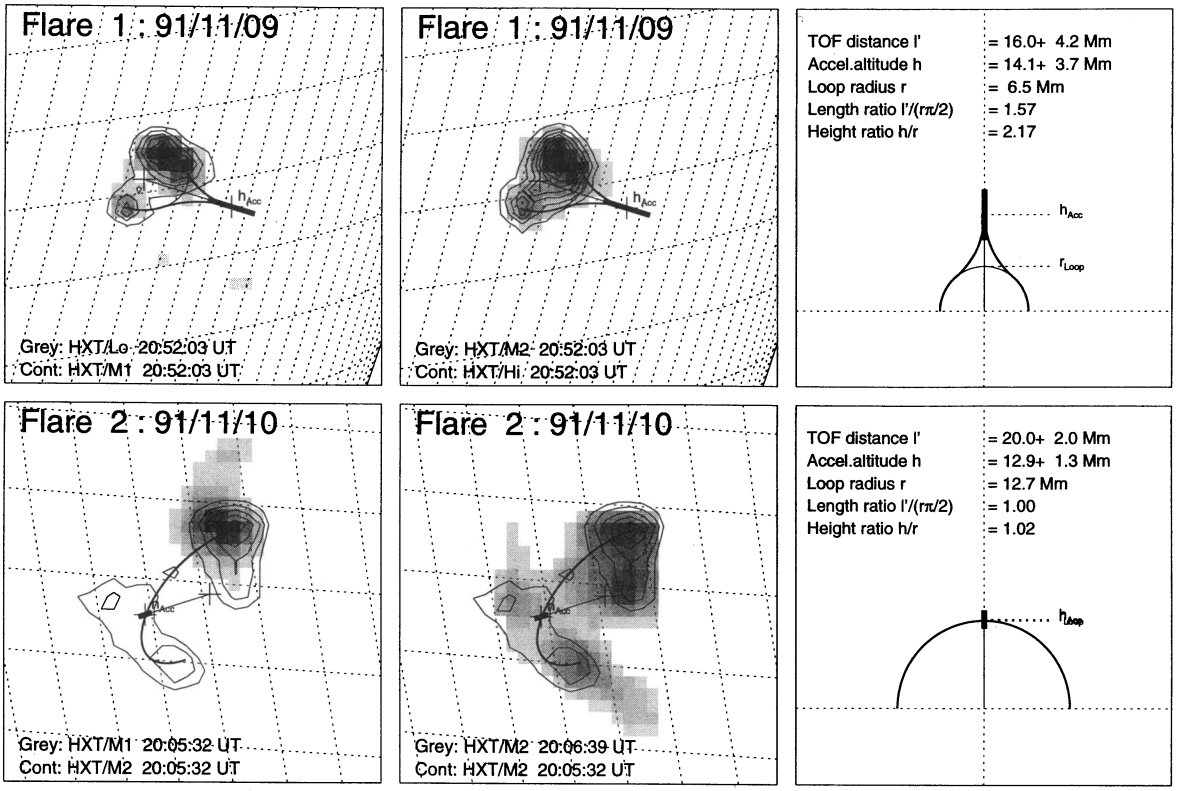

FIG. 10*a*

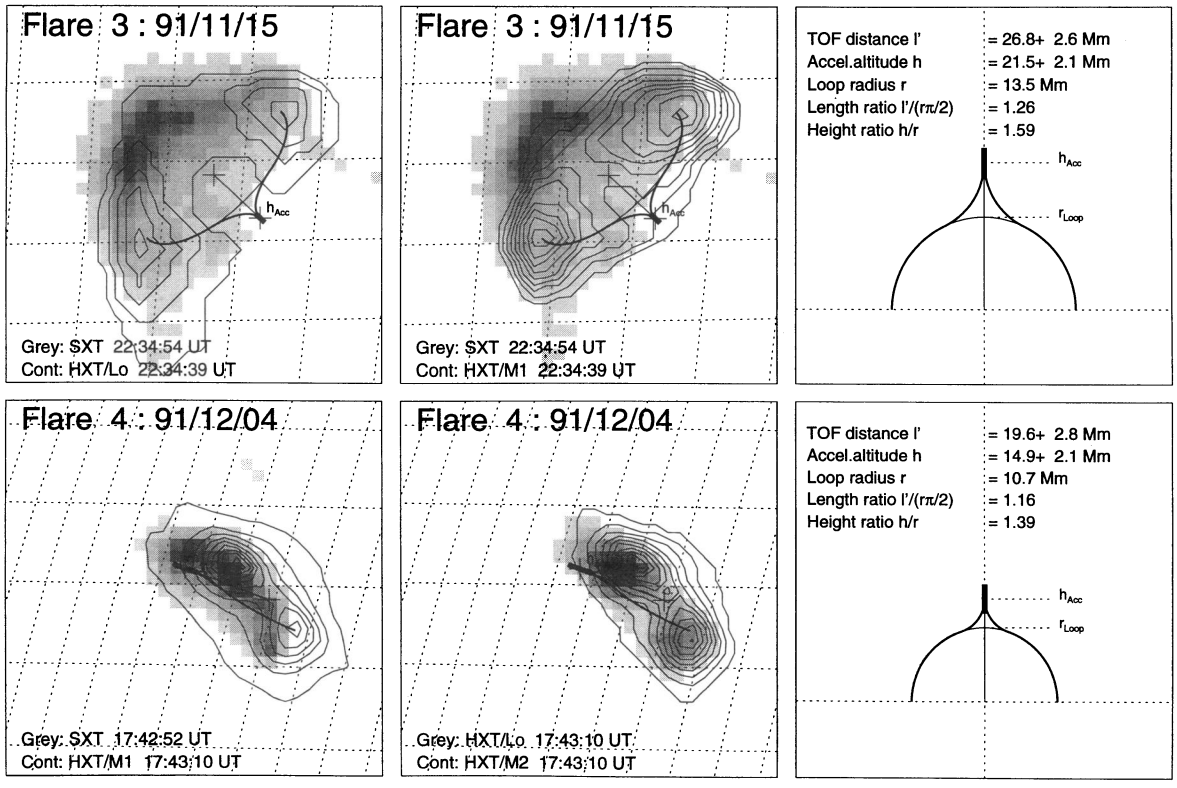

FIG. 10*b*

FIG. 10.—Overlays of coregistered HXT/Lo, M1, M2, Hi, and SXT images (*left and middle columns*), identified with date (*top*), start time (*bottom*), and instrument (*bottom*) for gray-scale plots (*gray*) and contour plots (*contours*). The contour levels are always linear, starting above the noise level. The HXR double footpoints are connected with a semicircular loop geometry in a vertical plane to the solar surface (*thin curve*). Symmetric open magnetic field lines joining the vertical in the cusp above the loop midpoints are projected in the same loop plane (*thick curves*). The length of the open field line corresponds to the TOF distance l', with the uncertainties $\pm\sigma_l$ indicated with a thick bar. A projection of the vertical loop plane is shown in the right columns. All panels have the same field of view (55,000 km), the spacing of the heliographic grid is 1° (12,150 km).

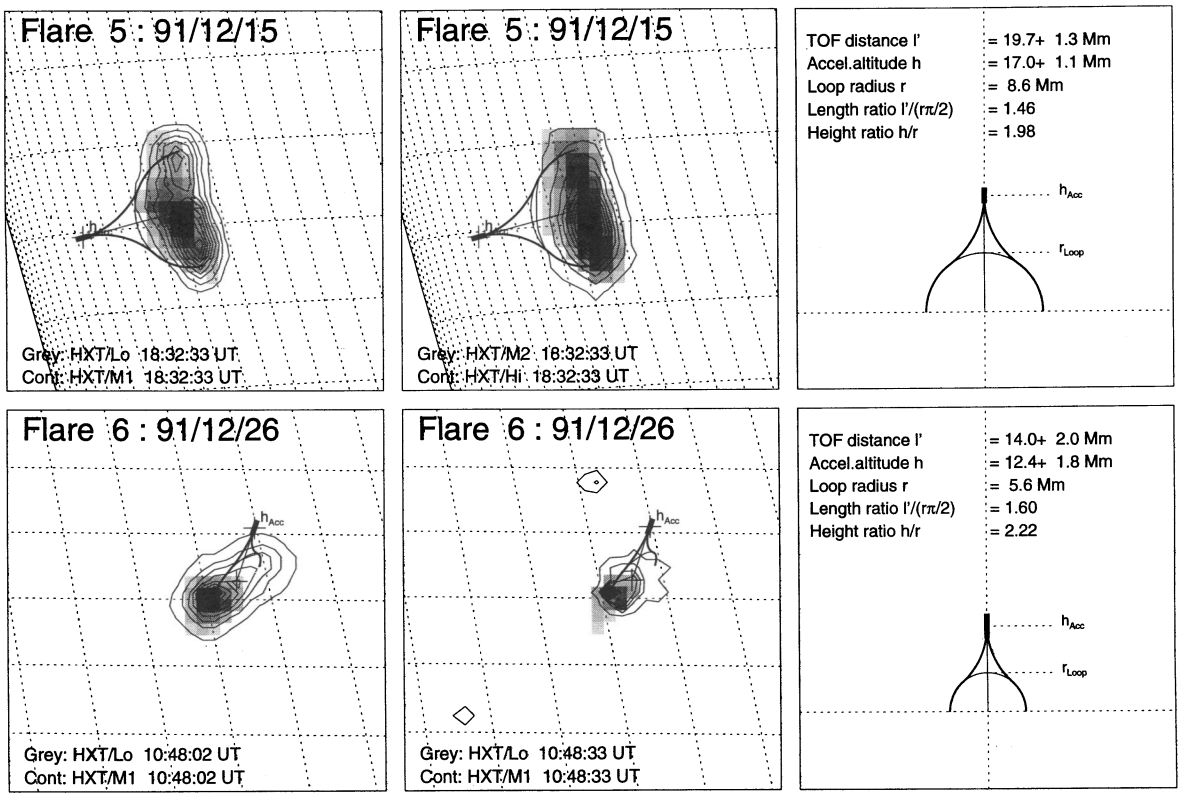

FIG. 10*c*

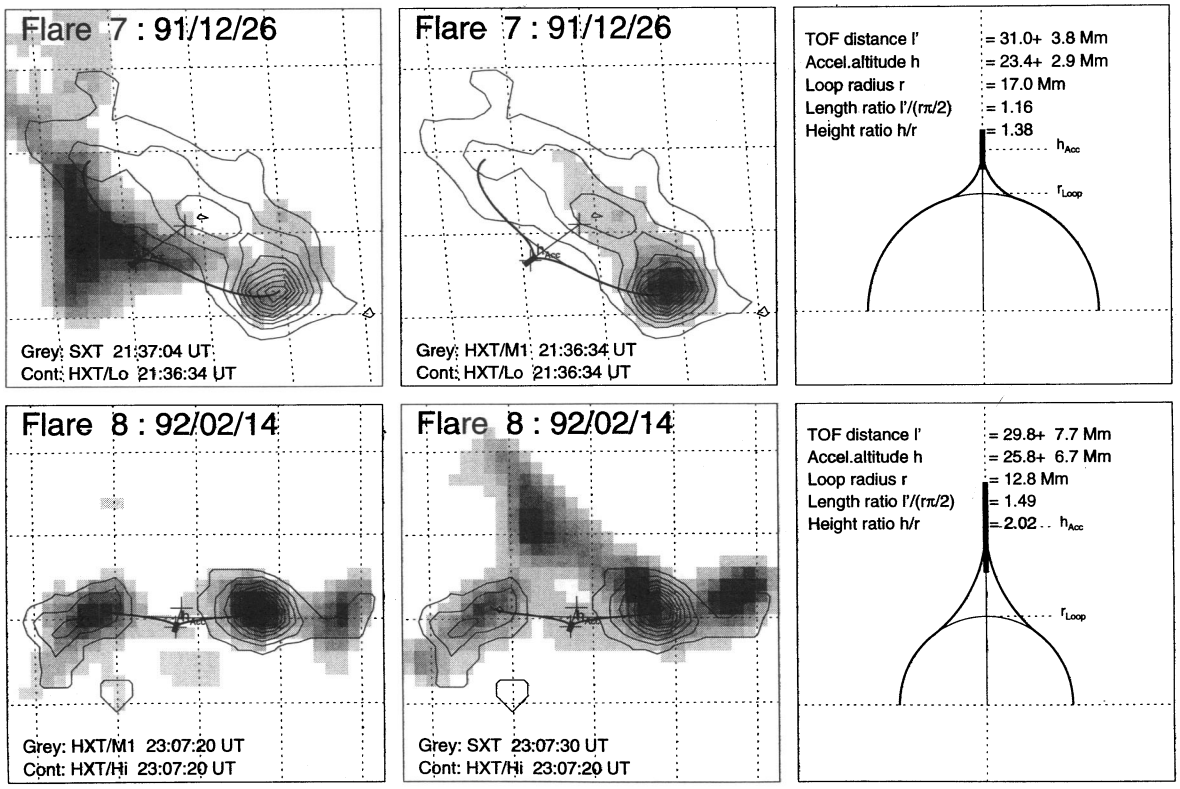

FIG. 10*d*

stream symmetrically toward the two footpoints, provided that the measured HXR delays are caused only by electron propagation time differences to the chromosphere. The uncertainties of the TOF-inferred heights $h \pm \sigma_h$ due to HXR photon noise (in the order of 4%–13%) are indicated with a thick bar on the vertical between the positions $h - \sigma_h$ and $h + \sigma_h$ in Figure 10. As an additional orientation we overlay also a heliographic grid with a grid spacing of 1°, corresponding to a distance of 12,150 km. All frames in Figure 10 (including the vertical projections) are shown on the same scale, with a field of view of 32 SXT pixels (=32 × 2.″46 = 79″ = 55,000 km). The measurements of the flare loop radii r and the inferred heights of the acceleration sites h are also listed in Figure 10 and Table 3.

3.3. *Descriptions of Individual Flares*

We describe here briefly some individual characteristics of the eight analyzed flares and provide references to literature (see also Table 3) where other aspects of these flares are investigated in more detail. A main source is the thesis of Sakao (1994), where seven of the eight flares selected here can be found. We also compile (in Table 3) during which flares SXR ejecta (four cases) and impulsive SXR footpoints (five cases) have been detected with SXT (from six cases).

Flare 1: 91/11/09, 2051 UT.—Sakao (1994, p.167) classifies the morphology of this HXR flare with four components. The HXT image in the highest channel (Hi: 53–93 keV; see Fig. 10) shows a clear double footpoint structure, where the northern parts splits into two subkernels at lower energies. This is the second smallest flare in our selection, with a footpoint separation of 13,000 km. Because of this small separation, no distinct SXR loop is seen in SXT, but an amorphous large blob centered at the apex of the inferred flare loop system.

Flare 2: 91/11/10, 2005 UT.—This is a relatively long-lasting flare (2005–2020 UT) peaking at 2009:25 UT. Sakao (1994, p.167) classifies the HXR source at the peak time as a single source, which is located about 30,000 km south of an initial HXR double footpoint system (shown in Fig. 10) identified during the TOF measurements at the flare's beginning (2005–2007). This is a typical case, where the *BATSE* burst trigger starts early, and the limited memory span of ≈3 minutes for the high-resolution MER data is not long enough to catch the flare peak. The system of bright SXR loops is rather extended and connects from the initial northern HXR double footpoints (shown in Fig. 10) to the southern HXR single source, which dominates during the flare peak (analyzed by Sakao 1994).

Flare 3: 91/11/15, 2234 UT.—This is probably one of the best studied flares, an X1.5 class flare, analyzed in HXRs (Sakao 1994; Sakao et al. 1992; Kane et al. 1993a, 1993b; McTiernan et al. 1994, using stereoscopic multispacecraft observations with *CGRO* and *Pioneer Venus Orbiter* [*PVO*]), nuclear lines (Kawabata et al. 1994a, 1994b), Ca XIX lines (Culhane et al. 1993), white light (Hudson et al. 1992), Hα and Ca lines (Canfield et al. 1992; Wuelser et al. 1994), and radio (Enome, see Fig. 6.3 in Sakao 1994).

The *Yohkoh HXT* flare mode triggered at 2234:38 UT, almost simultaneously with the *CGRO* burst trigger at 2234:36.6 UT. However, the MER data cover only the first ≈3 minutes (until 2237:20.4 UT), before the flare peaks (at 2237:36 UT). Moreover, the HXR time delay characteristics were found to evolve systematically during the early flare (see two episodes in Fig. 4), with TOF delays appearing only in the very early phase before 2236:00 UT, while HXR delays of opposite sign occur thereafter, indicating coronal trapping. Therefore, our *CGRO* TOF measurements apply only to the very early (precursor) flare phase, where a SXR loop is visible with an approximate footpoint separation of 27,000 km, straddling along the neutral line (see Fig. 3 in Canfield et al. 1992 or Fig. 2 in Wuelser et al. 1994). At the footpoints of this SXR loops, redshifted bright Hα kernels at Hα + 3.0 Å (Wuelser et al. 1994) and blueshifted Ca XIX lines (Culhane et al. 1993) were observed, indicating chromospheric evaporation driven by precipitating electrons during the early flare phase, which is exactly when we measure electron TOF differences with *CGRO*. The HXT/M1 image synthesized during the preflare phase (before 2236 UT; see Fig. 10) shows clearly a double footpoint structure with a separation of 27,000 km during the TOF measurements, leading to an acceleration height of $h = 21{,}500$ km in the preflare phase. This provides complementary information to the flare scenario developed by previous workers, who concluded that the flare starts with a large-scale magnetic reconfiguration that drives chromospheric evaporation by precipitating electrons in the preflare phase (based on the momentum balance between Hα and Ca XIX; Wuelser et al. 1994), involving a much larger loop system than the rather compact flare loop that develops later on and dominates the HXR emission during the impulsive flare phase (studied by Sakao 1994).

Flare 4: 91/12/04, 1743 UT.—This is a typical double footpoint flare loop (Sakao 1994, p.167) with almost symmetrically bright HXR sources. Although the SXR emission seems to be concentrated above the northern footpoint and lacking above the southern footpoint, it becomes clear from the projection in Figure 10 that the apex of the flare loop almost coincides with the northern footpoint for this particular line of sight.

Flare 5: 91/12/15, 1832 UT.—This flare was observed with HXT in flare mode, but SXT was pointing to another location with a brighter SXR target, so that we have only saturated full disk images from SXT available to constrain the location. Sakao (1994) does not classify the HXT morphology since he mistakenly judged that this flare occurred behind the limb. This is incorrect, however. The timing analysis of the *CGRO* data show the cleanest example of HXR delays that are fully consistent with electron TOF differences (Fig. 5) and thus provides clear evidence that the chromospheric footpoints can not be occulted by the limb. Actually, investigating the lower contours of the HXT/M1 channel (in Fig. 10), a double footpoint structure is evident. Because of the clean HXR delay measurements (thanks to the large modulation depth of the HXR pulses, see Fig. 1), the functional form of the HXR delays was also modeled in terms of combined electron propagation and acceleration timescales (with a null result, however; Paper V).

Flare 6: 91/12/26, 1047 UT.—This is the tiniest flare loop in our selection, with an estimated loop radius of $r = 5600$ km, based on the elliptical shape of the lowest HXT/H1 contours (Fig. 10). Sakao (1994) does not classify the morphology of this flare because no background data were available. For this smallest flare in HXT we find, interestingly, also the shortest electron TOF distances ($l' = 14{,}000 \pm 2000$ km).

Flare 7: 91/12/26, 2135 UT.—This flare shows a pronounced single HXR source (Sakao 1994) during the main impulsive phase. However, the lowest contours of the

HXT/M1 image outline a larger flare loop (with an estimated footpoint separation of 34,000 km) extending from the HXT single source in NE direction. The outlines of this flare loop are even clearer in the HXT/Lo and M1 images during the preflare, or in the SXT images during the impulsive phase. From the projection of a semicircular loop geometry (in Fig. 10) it becomes clear that the triangular feature in SXT corresponds to the cusp region, roughly coinciding with the acceleration site inferred from the electron TOF delays.

Flare 8: 92/02/14, 2306 UT.—This flare shows a rather complex morphology, with 3–4 HXT sources (Sakao 1994). Investigating the four HXT channels during the main impulsive phase we find three sources in the lower channels, but a simple double footpoint structure in the highest channel (Hi: 53–93 keV). The SXT images show a lambda-shaped structure, extending from the HXT/Hi double footpoints to the north, indicating a complex of loops. The multiple HXR components were also accompanied by impulsive SXR footpoint brightenings and white-light emission (Hudson, Driel-Gesztelyi, & Kosugi 1994).

3.4. *Summary of Results*

From the morphology of HXT and SXT images we identified in each of the eight analyzed flares a semicircular flare loop structure that is anchored in the HXR footpoint sources observed at energies of $\gtrsim 30$ keV, during flare episodes when *CGRO* data exhibit electron TOF delays. From the footpoint separation we determined the radius r of the flare loop, and projected the electron TOF distances l' in the vertical plane along an open field line that extends from the footpoints upward to the cusp region, ending at height h on the vertical. The results of the so-determined loop radii r and associated (projected) TOF distances l' are shown in Figure 11.

The prime result of this study is that we find a *tight correlation between the loop radius r* and the TOF distance l', following approximately the relation $l' \approx 2r$ (Fig. 11). Recall that the two parameters are measured completely independently, l' from temporal data with no spatial resolution versus r from spatial images with no temporal resolution. The two parameters are also measured by complete independent instruments, one from BATSE/*CGRO*, the other from HXT/*Yohkoh*. The correlation between the electron TOF distance l' and the loop radius r represents the first spatiotemporal relation found for relativistic particles in solar flares. Obviously, the electron TOF distance has a physical relation to the flare loop size. The ratio of the TOF distance l' to the loop radius r has a mean and a standard deviation of $l'/r = 2.1 \pm 0.4$. For the ratio of the TOF distance l' versus the loop half-length $s = r(\pi/2)$, we find an average ratio of $l'/s = 1.3 \pm 0.2$. This ratio should be 1 if the acceleration site is located exactly at the apex of the flare loop. If we assume that the excessive electron propagation path follows an open field line, we find a height ratio of $h/r = 1.7 \pm 0.4$ between the acceleration height h and the loop height r. All this relations hold for a range of flare loops that varies by a factor of 3, with loop radii from $r = 5600$ km to $r = 17{,}000$ km.

There is only one comparison with previous work, for the case of the Masuda flare on 1992 January 13, where a SXR loop radius of $r_{SXR} = 12{,}500$, a coronal HXR source in a height of $r_{HXR} = 22{,}100$ km, and an altitude of the acceleration site of $h = 44{,}000$ km were inferred (Paper III).

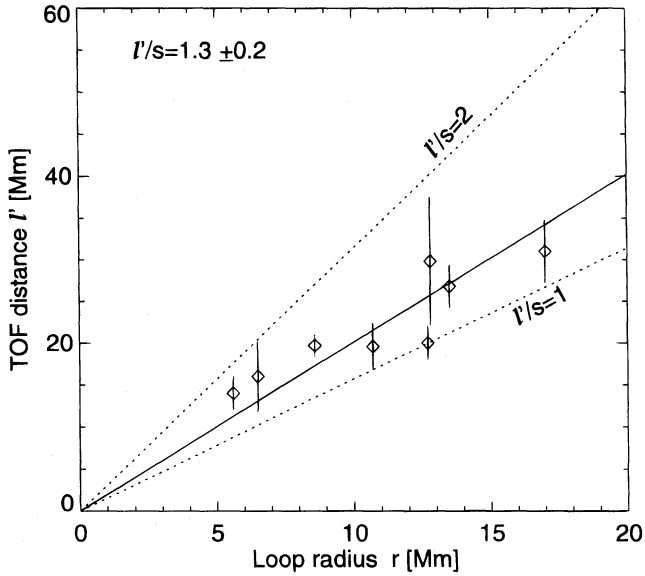

FIG. 11.—Relation between the (projected) TOF distance l' and the loop radius r. The (projected) TOF distance $l' = l * 0.54$ is directly measured from fitting the HXR time delays (see Fig. 5), while the loop radius r is measured from the angular separation of the HXR footpoints (corrected for the line-of-sight angle). Note the tight correlation between l' and r [or the loop half-length $s = r * (\pi/s)$], with an average ratio of $l'/s = 1.3 \pm 0.2$. For comparison, the loop half-length ($l'/s = 1$) and the loop full length ($l'/s = 2$) are also shown (*dashed lines*).

Depending on whether the SXR loop or the coronal HXR source is used as reference for the flare loop size, the height ratio is $h/r_{SXR} = 44{,}000$ km/12,500 km = 3.2 or $h/r_{HXR} = 44{,}000$ km/22,100 km = 2.0, respectively.

4. DISCUSSION

4.1. *Observational Constraints for Flare Models*

We analyzed a complete sample of flares, selected only by the criterion of large HXR fluxes ($C \geq 10^5$ counts s^{-1}) and the requirement of simultaneous time coverage between *CGRO* and *Yohkoh*. Thus, the selection should be representative among large flares, and moreover, the detection of fine structure and the high-precision timing analysis should not be biased or hampered by instrumental sensitivity limitations. In the following, we summarize the most important observational constraints and conclusions that emerge from this study, to be used as guidelines in future flare models.

1. Virtually all flares show *fine structure in HXR*, which can be characterized by quasi-periodic pulses with typical durations of $w_P \approx 0.5$–1.5 s, occurring during the preflare phase or the main impulsive phase, but which represent only a few percent of the total HXR flux. This pulsed HXR fine structure exhibits energy-dependent time delays in the order of $\tau(E) \lesssim 100$ ms, and the functional relation $\tau(E)$ was found to be fully consistent with electron TOF differences (in eight of the nine flares selected here).

2. The inferred *electron TOF distances* l', corrected for electron pitch angles and helicity of the magnetic field lines, were found in the range of $l' = 14{,}000$–$30{,}000$ km. The corresponding flare loops identified from the HXR footpoint separations in simultaneous *Yohkoh/HXT* images were found to have radii (or heights) of $r = 6500$–$17{,}000$ km. The TOF distance l' and the loop half-length $s = r * (\pi/2)$ were found to be proportional to each other, with a scale-

invariant ratio of $l'/s = 1.3 \pm 0.2$.

3. The inferred *electron propagation times* are in the range of $t^{\rm prop}(E) \approx 100$–$400$ ms (Table 2) for ≈ 60–400 keV electrons and correspond roughly to one loop transit time. The *pulsed HXR fine structure* must therefore be produced by electrons that precipitate directly to the footpoints without bouncing, while the smoothly varying HXR flux, which shows a distinctly different timing, must necessarily be produced by electrons with a different time history, most likely governed by magnetic mirroring and trapping.

4. The functional form of the energy-dependent HXR delays of the pulsed fine structure is fully consistent with propagation time differences within the uncertainties of the measurements (of a few ms here) and does not show any significant deviations that could indicate the involvement of finite *acceleration timescales*. This implies either extremely short acceleration times (of less than a few ms) or an energy-independent electron injection mechanism (e.g., via pitch-angle scattering) from an acceleration trap to the flare loop system (connected with the HXR footpoints).

5. We found also a correlation between *the duration of the HXR pulses* and the TOF distance (or loop size). This result implies that the modulation of the HXR pulses is controlled by a macroscopic parameter that is related to the flare loop size. A likely possibility is the role of fast (global) MHD oscillation modes, which have a period of $T = 2.6(d/v_{\rm A})$ (with $v_{\rm A}$ the Alfvén velocity and d the loop diameter) for a cylindrical flux tube (Roberts, Edwin, & Benz 1984). It is conceivable that such MHD oscillations in the environment of the acceleration region modulate the pitch angle of accelerated electrons, and control in this way their injection into the flare loop or their precipitation to the footpoints.

Based on these observational constraints we can try to identify suitable acceleration mechanisms and to pinpoint their location, specifically, whether acceleration takes place inside or outside the flare loop (e.g., in the cusp region). In the next two sections we discuss various acceleration models (grouped according to their location outside or inside the flare loop), specifically whether or not they are consistent with our inferred timing and electron TOF distances.

4.2. *Acceleration in the Cusp Region*

If the scale-invariant ratio of $l'/s = 1.3 \pm 0.2$ between the electron propagation path length l' and the loop half-length s is projected onto a magnetic field line that extends upward to the cusp region, we find a ratio of $h/r = 1.7 \pm 0.4$ for the average height of the centroid of the acceleration region, assuming a symmetric loop geometry. The HXR delay measurements are only sensitive to the position of the centroid of the acceleration region, while the spatial extent or the spatial fragmentation is largely undetermined because the modulation of the electron injection function is much longer ($w_P \approx 0.4$–1.6 s) than the propagation times ($t^{\rm prop} \approx 0.1$–0.4 s).

There are a number of flare scenarios with acceleration sites located in the cusp region; essentially all these scenarios are related to magnetic reconnection processes in an X-type, Y-type neutral point, or a current sheet above the flare loop (e.g., Sturrock 1966; Hirayama 1974; Kopp & Pneuman 1976; Shibata et al. 1995). Once magnetic reconnection starts, the process proceeds upward into the corona and forms new closed loops at successively higher levels (Kopp & Pneuman 1976). The brightest SXR flare loops, filled by chromospheric evaporation, thus (because of the filling delay with a typical timescale of $\lesssim 1$ minute) always appear at a lower altitude than the highest closed loops (beneath the Y-type neutral point), where electrons are accelerated, and drive subsequent evaporation by precipitation. This scenario not only explains why the acceleration site is always higher than the instantaneous brightest SXR flare loop (by a factor or $h/r = 1.7 \pm 0.4$ according to this study), but also why the directly precipitating electrons that drive chromospheric evaporation are not stopped in the dense plasma of the brightest SXR loops. A temporal sequence of this scenario is illustrated in Figure 12.

The cusp region above flare loops has now received increased attention motivated by a number of exciting new *Yohkoh* flare observations. Masuda (1994; Masuda et al. 1994, 1995) discovered HXR sources near the cusp region above the brightest SXR flare loops in energy bands up to $\lesssim 100$ keV. The origin of this cuspal HXR emission is difficult to understand for several reasons (Hudson & Ryan 1995), but could potentially be associated with the electron acceleration process. Shibata et al. (1996) identified in a sample of eight impulsive compact loop limb flares (including the Masuda 1992 January 13 flare) SXR plasma ejecta, which are interpreted as evidence for magnetic reconnection above the cusp region. In our sample, where six flares have been covered with SXT, we find SXR ejecta in four cases, and impulsive SXR footpoint brightenings in five cases (Table 3). Future analysis might reveal how close the irradiation center of the SXR ejecta (demarcating the position of the putative reconnection points) is located to the starting point of accelerated electrons (inferred here at an altitude of $h/r = 1.7 \pm 0.4$ from electron TOF measurements).

For the acceleration of electrons in the cusp region, a variety of acceleration mechanisms have been envisioned. In Sturrock's (1966) model electrons are stochastically accelerated in electric fields generated by the tearing mode instability in the cusp region. LaRosa & Moore (1993) proposed that an MHD turbulent cascade occurs in shear unstable Alfvénic outflows from different reconnection sites, which are suitable to accelerate electrons on subsecond timescales in a spatially fragmented way, by means of Fermi acceleration (LaRosa, Moore, & Shore 1994). Alternatively, Sakai & Ohsawa (1987) simulated particle acceleration in an explosive magnetic reconnection event, driven by the current loop coalescence, and found pulsating time structures on timescales comparable with the modulations observed here. Although the physical assumptions are quite different in these scenarios, they all can be operated in the cusp between a coronal reconnection site and a lower lying trapping flare loop, and are thus consistent with our finding of an average height of $h/r = 1.7 \pm 0.4$ above the SXR flare loop.

Another constraint found in our analysis is that the escape of energized electrons from the acceleration region does not show a dependence on the acceleration timescale, and thus, requires an escape or injection mechanism that is decoupled from the acceleration process. Particle acceleration can therefore operate in a continuous mode, while the escape of HXR-producing electrons is modulated on timescales of ≈ 1 s, e.g., by pitch angle scattering driven by MHD loop oscillations. A very similar situation was envisioned by LaRosa et al. (1994), where electrons are

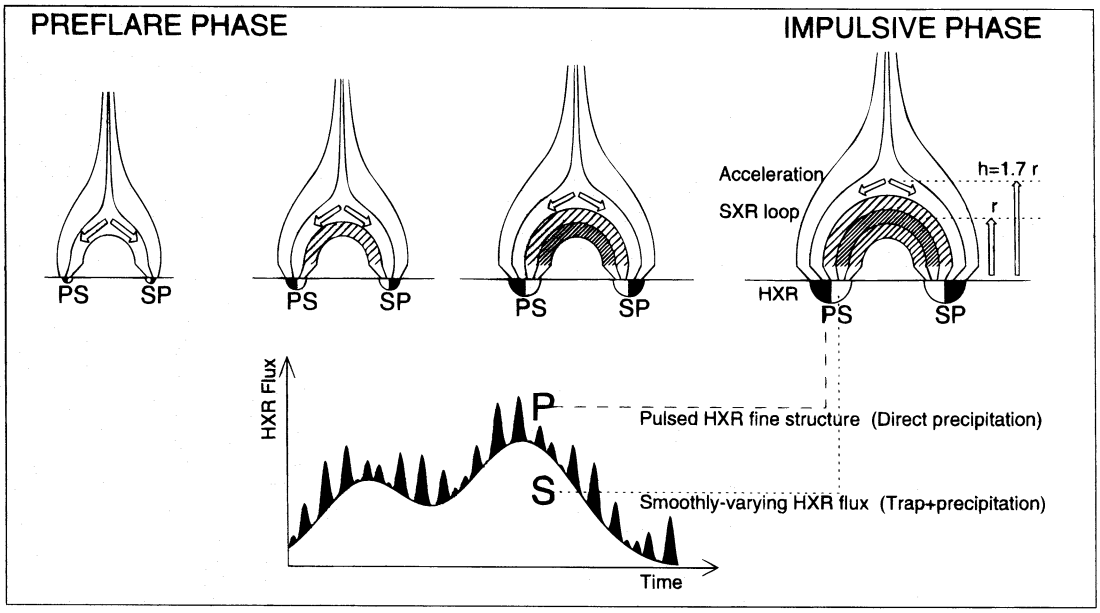

FIG. 12.—Proposed scenario with a *pulsed* and a *smooth* HXR flux component that can explain the observed HXR timing and the inferred acceleration heights. The *pulsed HXR fine structure* (*P*) is produced by electrons that are accelerated in the highest closed loops beneath the *Y*-type neutral point and precipitate directly without bouncing. Thus, their timing is determined by electron TOF differences. The *smoothly varying HXR flux* (*S*) is generated either by coronal (thin- or thick-target) energy loss during trapping, or by chromospheric thick-target emission after escaping. Note that the reconnection proceeds upward during the flare, and the brightest SXR loops appear, due to the filling delay by chromospheric evaporation, at a lower altitude (r) than the instantaneous electron acceleration site (h) located in the highest closed loops (at $h \approx 1.7r$).

Fermi accelerated in a magnetic mirror geometry and their escape is controlled by pitch-angle modulation.

4.3. *Acceleration inside the Flare Loop*

If the scale-invariant ratio of $l'/s = 1.3 \pm 0.2$ between the electron propagation path length l' and the loop half-length s is projected inside the loop, we find that the average propagation path makes up 65% of the total loop length. This mean value would also be consistent with an extended acceleration region covering 30%–100% of the total loop length. However, because many flares show double footpoint emission, a symmetric situation with unidirectional acceleration forces on both sides of the flare loop would be required to satisfy the measured electron TOF distances. An isotropic (e.g., stochastic) acceleration mechanism would produce two (oppositely directed) TOF distances, leading to two competing HXR delays of equal sign, weighted by the relative precipitation rates at the two footpoints. For strongly asymmetric mirror ratios (which are common; see Sakao 1994), the timing of electrons with the higher precipitation rate toward the footpoint with the weaker magnetic field would dominate. The acceleration source needs then to be located always at a location $65 \pm 10\%$ away from the weaker footpoint or $35 \pm 10\%$ close to the stronger footpoint, which would be a specific requirement for any theory. It also conflicts with Sakao's (1994) measurement of the simultaneity of the two HXR footpoint emissions within $\lesssim 100$ ms, at least for the larger loops where the observed electron propagation times are of order ≈ 300 ms. Hypothetically, one could also consider auroral acceleration mechanisms in *V*-potential drops of parallel electric fields (e.g., see recent observations by *Viking*; Louarn et al. 1990). Placing such upward directed electric fields above the footpoints of flare loops, we would expect electron TOF distances of $l'/s \lesssim 2$, which is somewhat larger than observed here.

The timing is different for *large-scale accelerating fields*, e.g., for electric DC field acceleration (Holman 1985; Tsuneta 1985; Emslie & Henoux 1995). We have to recall that we inferred the *projected TOF distance* l' based on the assumption of large pitch angles at arrival at the chromospheric footpoints, which is the most likely situation for free-streaming electrons in a flare loop with a large mirror ratio (because of the conservation of the magnetic moment). However, for electric DC field acceleration, electrons are not free-streaming and the magnetic moment is not conserved. A DC electric field acts only on the parallel moment, while the initial (thermal) perpendicular moment $v_\perp^{\rm th}$ is conserved. Consequently, the electron pitch angle becomes smaller and smaller with higher energies, i.e., $\sin \alpha(E) = v_\perp^{\rm th}/v(E)$. Therefore, we have to set the pitch angle correction to $q_\alpha = 1$ in the evaluation of the *electron acceleration distance* l''. Another difference to free-streaming electrons is that the average speed is only half of the final speed (in the nonrelativistic case), or a factor of $q_v = 0.44$ in the fully relativistic case for the relevant energy range here (see derivation and fits in Paper III). The electron acceleration distances l'' that correspond to the HXR delays observed here are thus $l'' = l'(q_v/q_\alpha) = l'(0.44/0.64) = l'0.69$. The length ratio of the electron flight path l'' to the loop half-length s is then $l''/s = 0.9 \pm 0.1$. This means that the accelerating electric DC field extends only from the footpoint to the apex, not along the entire loop.

There are more severe problems to reconcile large-scale electric DC field models with our observed HXR timing. For a constant electric field, all electrons would arrive simultaneously at the footpoints and produce a monoenergetic electron spectrum. One could consider various models where electrons entrain and leave the accelerating electric field channels at different places. Some of them are calculated and fitted to our HXR timing data in Paper V, but only one acceptable solution was found for the case of a

constant electric field. This situation requires a high electric field where electrons leave the current channels very quickly, so that the acceleration time is small compared with the propagation time, which corresponds to the TOF model. Alternatively, one could propose acceleration along current channels with different electric fields, a possibility suggested by Tsuneta (see discussion and modeling of this case in Paper III and V). This model produces a functional dependence of the (large-scale) acceleration time $t^{\rm acc}(E)$ on the final kinetic electron energy E,

$$t^{\rm acc}(\gamma) = \frac{l}{c}\sqrt{\frac{\gamma+1}{\gamma-1}} \quad (7)$$

[where γ is the Lorentz factor and $E = m_e c^2(\gamma - 1)$], which fits the HXT timing data equally well as the electron propagation time difference model $t^{\rm prop} = l/v(E)$. Thus, this model could theoretically account for the observed timing, if the extent of the accelerating field covers about a half-loop length ($l''/s = 0.9 \pm 0.1$). Additional problems of DC electric field models are that they cannot produce rapid fluctuations of order 1 s, as observed in the HXR pulses, because the rise times of inductive currents are considerably slower (estimated to be $\approx$30 s in Tsuneta 1995b). Another complication is that the energy range of HXR-producing electrons requires a similar large range of different electric fields, which in turn requires a large range of suitable Dreicer fields $E_{\rm D} \approx n_e/T$ for the same flare loop. Also, the predominance of very small pitch angles would produce a precipitation rate of almost 100%, which is difficult to reconcile with our finding that the bulk of HXR emission shows an opposite timing to the HXR pulses, consistent with a trapping mechanisms for the bulk of HXR-emitting electrons. Based on all these aspects, it appears that large-scale electric DC field models are difficult to reconcile with our HXR timing measurements.

5. CONCLUSIONS

Our high-precision timing analysis of HXR pulses in the 30–300 keV range in the eight largest flares simultaneously observed with BATSE/*CGRO* and HXT/*Yohkoh* demonstrated that the energy-dependent time delays can satisfactorily be fitted with a one-parameter model that includes only electron TOF differences. No significant deviation was found from this propagation time model that could indicate a possible dependence on acceleration timescales. The inferred electron TOF distances l' were compared with the loop half-lengths s observed in the HXT/*Yohkoh* images and a clear proportionality was found, yielding a scale-invariant ratio of $l'/s = 1.3 \pm 0.2$. If this length ratio is projected onto a magnetic field line that extends up to the cusp region, we find an average ratio of $h/r = 1.7 \pm 0.4$ for the height h of the acceleration site with respect to the flare loop radius r. This scale-invariant height ratio favors acceleration mechanisms operating in the cusp region, probably associated with magnetic reconnection processes above the flare loops. Models with large-scale electric DC fields, for which a length ratio of $l''/s = 0.9 \pm 0.1$ was inferred for the electron acceleration path length l'', are found difficult to reconcile with the observed HXR timing.

The *Yohkoh* data used in this paper were provided by the *Yohkoh* mission of ISAS, Japan, which was prepared and is operated by the international collaboration of Japanese, US, and UK scientists under the support of ISAS, NASA, and SERC, respectively. We are grateful to Taro Sakao and Jim McTiernan for developing the HXT-MULTIMG interface. The *CGRO* data were obtained through the Compton Observatory Science Support Center GOF account, provided by the NASA/Goddard Space Flight Center. We thank the *BATSE* P. I. team, G. Fishman, W. Paciesas, G. Pendleton, R. Wilson, C. Meegan, R. Preece at *MSFC*, and T. McGlynn at the *CGRO* science support center (GROSSC). The Solar Data Analysis Center at GSFC managed by J. Gurman is acknowledged for providing computational and database facilities. The work of M. J. A. was supported by SR&T grant NAG-5-2352, H. S. H. was supported by NASA grant NAS-8-37334, R. A. S. was supported by *CGRO* grant NAS-5-32584, and M. J. W. was supported by NASA cooperative agreement NCC 5-83 and NSF grant ATM-9400746.

REFERENCES

Aschwanden, M. J. 1996, in AIP Conf. Proc. 374, High-Energy Solar Physics, ed. R. Ramaty, N. Mandzhavidze, & X.-M. Hua (New York: AIP), 300 (Paper V)
Aschwanden, M. J., Hudson, H., Kosugi, T., & Schwartz, R. A. 1996, ApJ, 464, 985 (Paper III)
Aschwanden, M. J., Montello, M. L., Dennis, B. R., & Benz, A. O. 1995a, ApJ, 440, 394
Aschwanden, M. J., & Schwartz, R. A. 1995, ApJ, 455, 699 (Paper II)
———. 1996, ApJ, 464, 974 (Paper IV)
Aschwanden, M. J., Schwartz, R. A., & Alt, D. M. 1995b, ApJ, 447, 923 (Paper I)
Brown, J. C. 1971, Sol. Phys., 18, 489
Canfield, R. C., et al. 1992, PASJ, 44, L111
Culhane, J. L., et al. 1993, Adv. Space Res., 13, no. 9, 303
Dennis, B. R. 1985, Sol. Phys., 100, 465
———. 1988, Sol. Phys., 118, 49
Dennis, B. R., & Schwartz, R. A. 1989, Sol. Phys., 121, 75
Dennis, B. R., & Zarro, D. M. 1993, Sol. Phys., 146, 177
Duijveman, A., Hoyng, P., & Machado, M. E. 1982, Sol. Phys., 81, 137
Emslie, A. G. 1978, ApJ, 224, 241
———. 1983, ApJ, 271, 367
Emslie, A. G., & Henoux, J. C. 1995, ApJ, 446, 371
Emslie, A. G., & Mehta, S. 1994, EOS Suppl., 1994 April 19, 295
Fishman, G. J., et al. 1989, in Proc. *GRO* Science Workshop, The Burst and Transient Source Experiment (BATSE)—Scientific Objectives and Capabilities, ed. W. N. Johnson (Greenbelt: NASA GSFC), 2-39
Fishman, G. J., Meegan, C. A., Wilson, R. B., Paciesas, W. S., & Pendleton, G. N. 1992, in The Compton Observatory Science Workshop, ed. C. R. Shrader, N. Gehrels, & B. R. Dennis (NASA CP 3137), 26
Hirayama, T. 1974, Sol. Phys., 34, 323
Holman, G. D. 1985, ApJ, 293, 584
Hoyng, P., et al. 1981, ApJ, 244, L153
Hudson, H. S., Acton, L. W., Hirayama, T., & Uchida, Y. 1992, PASJ, 44, L77
Hudson, H. S., & Ryan, J. 1995, ARA&A, 33, 239
Hudson, H. S., van Driel-Gesztelyi, L., & Kosugi, T. 1994, in NRO Rep. 360, Proc. Kofu Symp. ed. S. Enome & T. Hirayama (Tokyo: National Astronomical Observatory), 397
Inda-Koide, M., Makishima, K., Kosugi, T., & Kaneda, H. 1995, PASJ, 47, 661
Kane, S. R., Hurley, K., McTiernan, J. M., & Sommer, M. 1993a, Adv. Space Res., 13/9, 241
Kane, S. R., McTiernan, J. M., Loran, J., Lemen, J., Yoshimori, M., Ohki, K., Kosugi, T. 1993b, Adv. Space Res., 13/9, 237
Kawabata, K., Yoshimori, M., Suga, K., Morimoto, K., Hiraoka, T., Sato, J., & Ohki, K. 1994a, ApJS, 90, 701
———. 1994b, in NRO Rep. 360, Proc. Kofu Symp., ed. S. Enome & T. Hirayama (Tokyo: National Astronomical Observatory), 123
Kopp, R. A., & Pneuman, G. W. 1976, Sol. Phys., 50, 85
Kosugi, T., et al. 1991, Sol. Phys., 136, 17
LaRosa, T. N., & Moore, R. L. 1993, ApJ, 418, 912
LaRosa, T. N., Moore, R. L., Miller, J. A., & Shore, S. N. 1995, ApJ, in press
LaRosa, T. N., Moore, R. L., & Shore, S. N. 1994, ApJ, 425, 856
Louarn, P., Roux, A., de Feraudy, H., & Le Queau, D. 1990, J. Geophys. Res., 95/A5, 5983
Masuda, S. 1994, Ph.D. thesis, National Astron. Obs., Univ. Tokyo, Mitaka/Tokyo

Masuda, S., Kosugi, T., Hara, H., Sakao, T., Shibata, K., & Tsuneta, S. 1995, PASJ, 47/5, 677
Masuda, S., Kosugi, T., Hara, H., Tsuneta, S., & Ogawara, Y. 1994, Nature, 371, no. 6497, 495
McTiernan, J. M., Kane, S. R, Hurley, K., Laros, J. G., Fenimore, E. E., Klebesadel, R. W., Sommer, M., & Yoshimori, M. 1994, in NRO Rep. 360, Proc. Kofu Symp., ed. S. Enome & T. Hirayama (Tokyo: National Astronomical Observatory), 389
Roberts, B., Edwin, P. M., & Benz, A. O. 1984, ApJ, 279, 857
Sakai, J. I., & Ohsawa, Y. 1987, Space Sci. Rev., 46, 113
Sakao, T., et al. 1992, PASJ, 44, L83
———. 1994, Ph.D. thesis, National Astron. Obs., Univ. Tokyo, Mitaka/Tokyo
Shibata, K., Masuda, S., Shimojo, M., Hara, H., Yokoyama, T., Tsuneta, S., Kosugi, T., & Ogawara, Y. 1996, ApJ, 451, L83
Shibata, K., Masuda, S., Shimojo, M., Yokoyama, T., Tsuneta, S., Kosugi, T., & Ogawara, Y. 1995, ApJ, 451, L83
Sturrock, P. A. 1966, Nature, 211, 695
Takakura, T., Tanaka, K., & Hiei, E. 1984, Adv. Space Res., 4, 143
Tsuneta, S. 1985, ApJ, 290, 353
———. 1995a, ApJ, 456, 840
———. 1995b, PASJ, 47, 691
Tsuneta, S., et al. 1991, Sol. Phys., 136, 37
Yoshimori, M., et al. 1992, PASJ, 44, L51
———. 1994, ApJ, 424, 459